Experimental investigation of the energy extraction by a fully-passive flapping-foil hydrokinetic turbine prototype

Matthieu Boudreau[a,1], Guy Dumas[a,2], Mostafa Rahimpour[b], Peter Oshkai[b]

[a] *CFD Laboratory LMFN, Département de génie mécanique, Université Laval, Québec, QC, Canada, G1V 0A6*
[b] *Department of Mechanical Engineering, University of Victoria, Victoria, BC, Canada, V8W 2Y2*

Postprint, 2018 - Journal of Fluids and Structures
Published version available online at: https://doi.org/10.1016/j.jfluidstructs.2018.07.014

Abstract

Experiments were conducted to assess the performance of a fully-passive flapping-foil hydrokinetic turbine for which the self-induced and self-sustained blade motions are resulting from the interaction between the blade's elastic supports (springs and dampers) and the flow field. Previous numerical studies have shown that such a turbine can extract a substantial amount of energy from the flow while offering the possibility to simplify the complex mechanical apparatus generally needed to constrain and couple the blade pitching and heaving motions in the case of the conventional fully-constrained flapping-foil turbine. Based on these promising numerical investigations, a prototype was designed and tested in a water channel at a chord Reynolds number of 21 000. Robust and periodic motions of large amplitudes were observed leading to an energy harvesting efficiency reaching 31% and a power coefficient of 0.86. The sensitivity of the turbine dynamics to seven different structural and inflow parameters was evaluated experimentally around a baseline case achieving a high level of performance. It was found that the turbine maintains a good performance over a large range of parameters.

Keywords: Passive, Oscillating foil, Power generation, Fluid-structure interaction, Divergence

1. Introduction

The flapping-foil turbine concept is one of the various innovative and promising sources of clean and renewable energy that have received an increased attention during the last decade (Young et al., 2014; Xiao and Zhu, 2014). It consists in one or multiple blades undergoing both pitching (rotational) and heaving (translational) motions with a swept area that is perpendicular to the flow. Although it would also be possible for these turbines to extract energy from the wind, they have mostly been developed as hydrokinetic turbines, which extract energy from rivers or tidal currents. The flapping-foil turbine concept has proven to be competitive with the horizontal-axis and vertical-axis turbine technologies, with efficiencies exceeding 40% (Kinsey et al., 2011; Kinsey and Dumas, 2012, 2014; Young et al., 2014; Xiao and Zhu, 2014).

In order to reach such a good level of performance, the designers have, in the past, mechanically coupled and constrained the two motions through complex mechanisms, hence making the turbine a single-degree-of-freedom (1-DOF) device (McKinney and DeLaurier, 1981; Kinsey et al., 2011; Xu et al., 2017). This approach allows prescribing the amplitudes and the frequencies of the heaving and pitching motions as well as the phase lag between them. However, several issues can arise from this complexity. First, a significant amount of energy can be lost before being converted into electricity. For example, Kinsey et al. (2011) reported that 25% of the power extracted from the flow by their fully-constrained flapping-foil turbine was lost before reaching the electric generator due to the friction between the different moving components forming the coupling mechanism. Moreover, complex mechanical assemblies are usually prone to a higher risk of failure in addition to being more expensive.

[1] matthieu.boudreau.1@ulaval.ca
[2] gdumas@gmc.ulaval.ca

Instead of optimizing the coupling mechanism, a more fundamental change has been proposed: the mechanism can simply be removed! One possible way to achieve this is to use an independent actuator for the pitching motion (Kim et al., 2017), making the concept a two-degree-of-freedom (2-DOF) turbine. Let us recall here that efficient flapping-foil turbines usually require only a small amount of energy to drive the pitching motion on a cycle-averaged basis, while the heaving motion accounts for the net energy extraction (Kinsey and Dumas, 2008, 2014; Zhu, 2011). Such a 2-DOF turbine does not necessitate rigid mechanical links to couple the heaving and the pitching motions, but needs a dedicated actuator for the pitching motion, controllers for both degrees of freedom and an electric generator connected to the heaving motion. Moreover, the electric generator of such a turbine may need to act as an actuator at some instants during the turbine blade cycle in order to prescribe the desired heaving motion. Therefore, this motion-constrained strategy still results in a relatively complex apparatus.

Several authors proposed a simplification to the aforementioned 2-DOF version of the flapping-foil turbine by considering a free or passive heaving motion (Abiru and Yoshitake, 2011, 2012; Deng et al., 2015; Derakhshandeh et al., 2016; Griffith et al., 2016; Huxham et al., 2012; Shimizu et al., 2008; Sitorus et al., 2015; Teng et al., 2016; Wu et al., 2014, 2015; Zhan et al., 2017; Zhu et al., 2009; Zhu and Peng, 2009). More specifically, this scenario involves a blade that is elastically supported in heave instead of being connected to the turbine structure with rigid links. One consequence of this simplification is that the heaving motion cannot be prescribed, but rather solely relies on the interaction between the elastically-supported foil and the flow. The heaving motion is thus self-induced and self-sustained. Two-dimensional (2D) numerical studies (Deng et al., 2015; Teng et al., 2016) and experimental works (Abiru and Yoshitake, 2011, 2012; Huxham et al., 2012) reported efficiencies exceeding 30% and 20%, respectively. This "semi-passive" turbine concept does not need a controller in heave and a simpler form of energy-extracting device (generator) can be used. Indeed, since the heaving motion is free, the energy-conversion device never has to act as an actuator. It corresponds in this case to an energy sink throughout the turbine blade cycle. This device could still be an electric generator in order to convert the energy extracted from the flow into electricity, but other possibilities also arise, such as using the flapping-foil turbine concept as a reciprocating pump (Farthing, 2013). However, both an actuator and a controller are still needed to prescribe the pitching motion.

A further simplification, for which both degrees of freedom are decoupled and elastically supported, was first proposed by Peng and Zhu (2009). This is referred to as a fully-passive flapping-foil turbine. For a given flow, they observed four different types of responses depending on the structural parameters characterizing the elastically-supported foil. Among them, only one was suitable for a stable and efficient energy extraction. This response was characterized by periodic pitching and heaving motions with large amplitudes and it led to an efficiency of 20% and a power coefficient of about 0.3. The other responses were either irregular, thereby negatively affecting the predictability and the controllability of the energy extraction, or the foil remained stationary at its equilibrium position and did not extract any energy from the flow. Zhu (2012) demonstrated that the presence of shear in the inflow could lead to new undesired types of responses and, more importantly, could restrict the parameter range for which useful large-amplitude periodic motions are observed. Wang et al. (2017) later found that this parameter range is also affected by the pitch axis location and that a pitch axis located at 0.35 chord length from the leading edge was optimal in their case.

The above-cited studies performed by Peng and Zhu (2009), Zhu (2012) and Wang et al. (2017) have all been conducted in the laminar regime ($\mathrm{Re} = 1\,000$ and $\mathrm{Re} = 400$). Veilleux and Dumas (2017) carried out 2D numerical simulations at a much larger Reynolds number of 500 000 using the Spalart-Allmaras URANS turbulence model (Spalart and Allmaras, 1994), which is more representative of the operation of full-scale turbines. As in the works of Peng and Zhu (2009) and Zhu (2012), Veilleux and Dumas (2017) observed different responses of the foil, including large-amplitude periodic motions. Following an optimization process, they obtained a turbine efficiency reaching 29.1% and a power coefficient of 0.935. Furthermore, they pointed out that an adequate synchronization between the pitching and heaving motions is crucial for an optimal energy extraction by fully-passive flapping-foil turbines, as is also the case for their fully-constrained counterparts (Xiao and Zhu, 2014; Young et al., 2014).

While the aforementioned studies reported good results from 2D numerical simulations, the same level of performance has yet to be observed experimentally with a fully-passive flapping-foil turbine prototype. Similar devices have been studied previously but these works did not focus on the energy extraction performance (Amandolese et al., 2013; Pigolotti et al., 2017). Such a prototype has therefore been designed for the present work and has been tested in a water channel with the objective of proving the feasibility and confirming the potential of the fully-passive flapping-foil turbine concept. The current study also evaluates the sensitivity of the turbine performance to the variation of

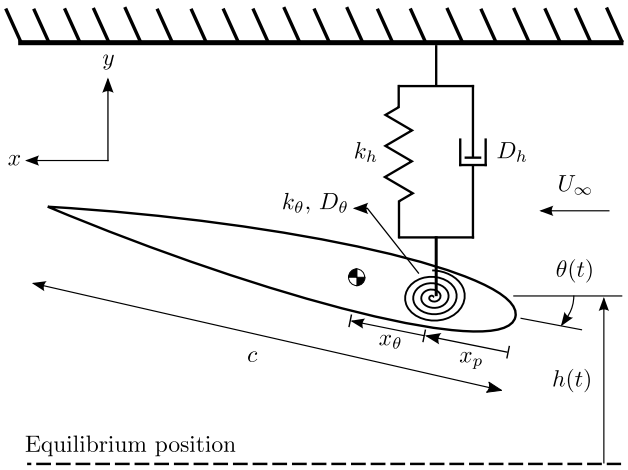

Figure 1: Outline of the fully-passive flapping-foil turbine concept.

several governing parameters. The fully-passive concept, the experimental setup and the measurement methodology are described in Section 2, while the analysis of a baseline case and the results of a parametric study are presented in Section 3.

2. Methodology

2.1. The fully-passive flapping-foil turbine concept

The fully-passive flapping-foil turbine concept considered in this study is similar to the one described in the work of Veilleux and Dumas (2017). As shown in Fig. 1, it consists in a rigid blade elastically supported by springs in heave and in pitch as well as by a damper in heave. This damper models the energy sink that would result, for example, from the energy conversion into electricity by an electric generator. The blade is free to pitch ($\theta(t)$) about a pitch axis located at a distance x_p from the leading edge and to heave ($h(t)$) in the y-direction. The motions are restricted to these two degrees of freedom (DOF) and gravity acts in the span direction, or z-direction, hence playing no role in the blade dynamics. Unlike the turbine analyzed by Veilleux and Dumas (2017), no pitch damper is explicitly used in the current study. However, due to the inherent presence of friction in a real experimental setup, some undesired viscous pitch damping ($D_{\theta,\mathrm{v}}$) is inevitably present and must be considered in addition to some viscous heave damping ($D_{h,\mathrm{v}}$) as well as some Coulomb friction (dry friction) both in heave ($F_{y\,\mathrm{Coulomb}}$) and in pitch ($M_{\,\mathrm{Coulomb}}$). As a result, the total linear heave damping coefficient (D_h) is the sum of the desired energy sink ($D_{h,\mathrm{e}}$), corresponding to the energy that could be converted into electricity, and the viscous damping stemming from the additional undesired friction in heave ($D_{h,\mathrm{v}}$):

$$D_h = D_{h,\mathrm{e}} + D_{h,\mathrm{v}} \,, \tag{1}$$

while the total linear pitch damping coefficient (D_θ) simply corresponds to the undesired viscous damping in pitch:

$$D_\theta = D_{\theta,\mathrm{v}} \,. \tag{2}$$

Because of the presence of Coulomb friction in the experimental setup and the use of a different sign convention for θ, the equations of motion are slightly different than those presented by Veilleux and Dumas (2017). They are given here in their dimensionless form:

$$C_{F_y}/2 \;=\; m_h^*\,\ddot{h}^* \;+\; S^*\left(\ddot{\theta}^*\cos\theta - \dot{\theta}^{*2}\,\sin\theta\right) + \;D_h^*\,\dot{h}^* \;+\; k_h^*\,h^* \;+\; C_{F_{y\,\mathrm{Coulomb}}}/2\,, \tag{3}$$

$$C_M/2 \;=\; I_\theta^*\,\ddot{\theta}^* \;+\; S^*\ddot{h}^*\cos\theta \;+\; D_\theta^*\,\dot{\theta}^* \;+\; k_\theta^*\,\theta + \;C_{M_{\,\mathrm{Coulomb}}}/2\,, \tag{4}$$

where the superscript $(\cdot)$ denotes differentiation with respect to time and:

$$C_{F_y} = \frac{F_y}{0.5\,\rho\,U_\infty^2\,b\,c}\ ,\quad C_M = \frac{M}{0.5\,\rho\,U_\infty^2\,b\,c^2}\ ,\ C_{F_{y\,\mathrm{Coulomb}}} = \frac{F_{y\,\mathrm{Coulomb}}}{0.5\,\rho\,U_\infty^2\,b\,c}\ ,\quad C_{M_{\mathrm{Coulomb}}} = \frac{M_{\mathrm{Coulomb}}}{0.5\,\rho\,U_\infty^2\,b\,c^2}\ ,$$

$$m_h^* = \frac{m_h}{\rho\,b\,c^2}\ ,\quad I_\theta^* = \frac{I_\theta}{\rho\,b\,c^4}\ ,\quad S^* = \frac{S}{\rho\,b\,c^3}\ ,\ D_h^* = \frac{D_h}{\rho\,U_\infty\,b\,c}\ ,\quad D_\theta^* = \frac{D_\theta}{\rho\,U_\infty\,b\,c^3}\ ,\quad k_h^* = \frac{k_h}{\rho\,U_\infty^2\,b}\ ,\quad k_\theta^* = \frac{k_\theta}{\rho\,U_\infty^2\,b\,c^2}\ ,$$

$$h^* = \frac{h}{c}\ ,\quad \dot{h}^* = \frac{\dot{h}}{U_\infty}\ ,\quad \ddot{h}^* = \frac{\ddot{h}\,c}{U_\infty^2}\ ,\ \dot{\theta}^* = \frac{\dot{\theta}\,c}{U_\infty}\ ,\quad \ddot{\theta}^* = \frac{\ddot{\theta}\,c^2}{U_\infty^2}\ .$$

The definitions of all the parameters involved in the equations of motion as well as those shown in Fig. 1 are provided in Table 1. Details about the derivation of the dimensionless equations can be found in the work of Veilleux (2014).

Table 1: List of the parameters involved in the equations of motion.

Symbol	Units	Definition
b	[m]	Blade span length
c	[m]	Chord length
ρ	[Kg/m^3]	Water density
U_∞	[m/s]	Freestream velocity
h	[m]	Heave position of the pitch axis (upward positive in Fig. 1)
θ	[rad]	Pitch angle (clockwise positive in Fig. 1)
t	[s]	Time
x_p	[m]	Distance between the leading edge and the pitch axis
x_θ	[m]	Distance between the pitch axis and the center of mass (defined positive when the pitch axis is upstream of the center of mass)
F_y	[N]	Hydrodynamic force component in the heave (y) direction
M	[N·m]	Hydrodynamic moment about the pitch axis
$F_{y\,\mathrm{Coulomb}}$	[N]	Coulomb friction force component in the heave (y) direction
M_{Coulomb}	[N·m]	Coulomb friction moment about the pitch axis
m_h	[Kg]	Mass of all the components undergoing the heaving motion
I_θ	[Kg·m^2]	Moment of inertia about the pitch axis
S	[Kg·m]	Static moment (mass of the components only undergoing the pitching motion times x_θ)
D_h	[N·s/m]	Total linear heave damping coefficient
$D_{h,\mathrm{e}}$	[N·s/m]	Linear heave damping coefficient of the eddy-current brake (desired energy sink)
$D_{h,\mathrm{v}}$	[N·s/m]	Linear heave damping coefficient of the heave bearings
D_θ	[N·m·s/rad]	Linear pitch damping coefficient of the pitch bearings
k_h	[N/m]	Heave stiffness coefficient
k_θ	[N·m/rad]	Pitch stiffness coefficient

The two nonlinear equations of motion (Eqs. 3 and 4) are coupled both via the coupling between the hydrodynamic force and moment and the inertial coupling terms, i.e., the terms involving the static moment S^*[3]. However, the inertial

[3]This parameter was referred to as the static imbalance in the work of Veilleux (2014); Veilleux and Dumas (2017).

coupling terms only play a role when the static moment is not zero, i.e., when the center of mass does not coincide with the pitch axis. It is worth recalling that there are no mechanical links between the heaving and the pitching motions that could enforce a particular relation between these two degrees of freedom. In other words, the motion shapes, the amplitudes, the frequencies and the phase lag between the heaving and the pitching motions are not imposed.

For a given flow, there are 9 structural parameters playing a role in the turbine dynamics explicitly appearing in Eqs. 3 and 4, namely:

$$C_{F_{y\,\mathrm{Coulomb}}}, \qquad C_{M_{\mathrm{Coulomb}}}, \qquad m_h^*, \qquad I_\theta^*, \qquad S^*, \qquad D_h^*, \qquad D_\theta^*, \qquad k_h^* \quad \text{and} \quad k_\theta^*,$$

in addition to the position of the pitch axis (x_p/c) for a total of 10 governing structural parameters. The challenge of designing a fully-passive flapping-foil turbine therefore consists in finding adequate values for these 10 parameters that result in useful motions in terms of energy extraction, i.e., periodic motions of large amplitudes, with a single frequency for both degrees of freedom and an appropriate phase lag between the heaving motion and the pitching motion.

2.2. Experimental setup

The experiments were carried out in the water channel of the Fluid Mechanics Laboratory at the University of Victoria, BC, Canada. Its test section has a cross section of 0.45 m by 0.45 m and a length of 2.5 m. The fully-passive flapping-foil turbine prototype is composed of non-moving components, components only undergoing the heaving motion and components undergoing both the heaving and the pitching motions, indicated by different colors in Fig. 2. These different components can also be observed in Fig. 3, which shows the blade at two different positions during a given test in the water channel.

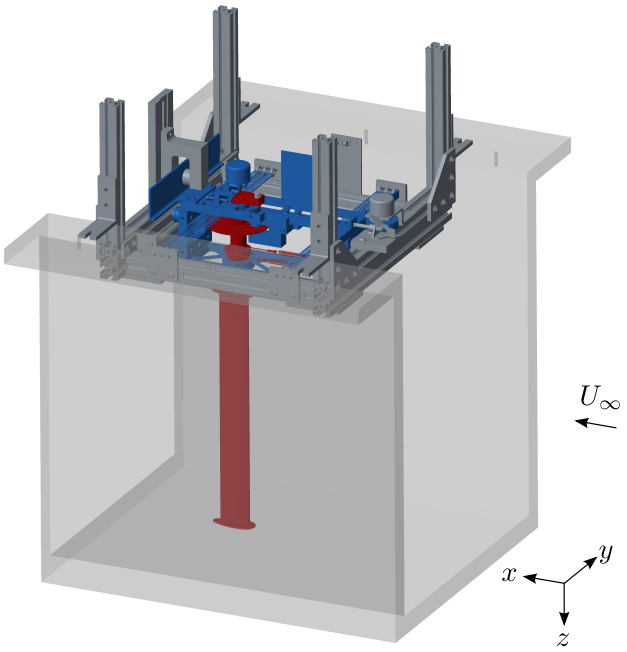

Figure 2: 3D model of the turbine prototype showing the non-moving components in gray, the components only undergoing the heaving motion in blue and the components undergoing both the heaving and the pitching motions in red. (For interpretation of the references to color in this figure legend, the reader is referred to the web version of this article.)

A carriage is mounted on linear guided roller bearings, thereby allowing it to move in the heave (transverse) direction. The top end of the blade is attached to a shaft, which is itself free to rotate while moving with the heaving carriage. The turbine blade is straight, its cross section corresponds to a symmetric NACA0015 profile with a 50 mm chord length and the pitch axis is located at the third-chord point ($x_p/c = 1/3$). In order to minimize the tip losses, end plates are placed at both ends of the blade. Moreover, the distance between the free extremity of the blade and the

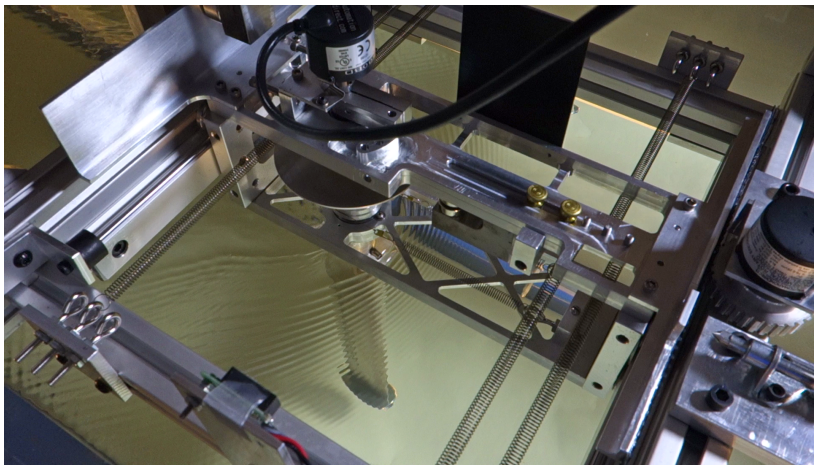

(a) $h/c = 0$ and $\theta = 0°$ (equilibrium position).

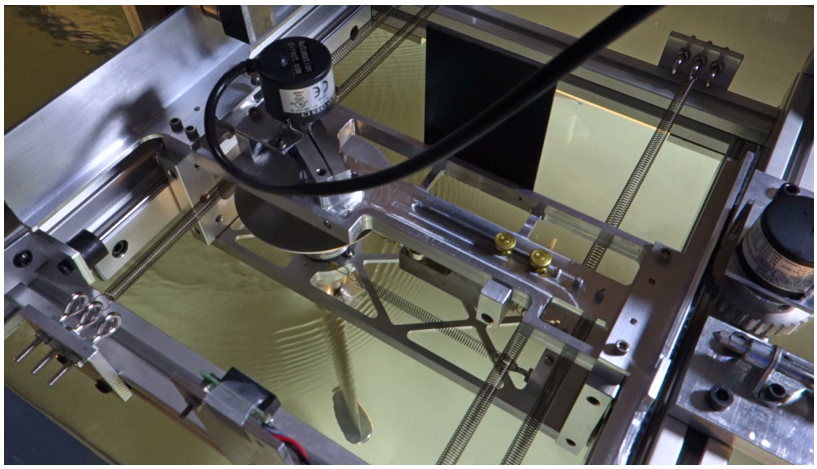

(b) $h/c \neq 0$ and $\theta \neq 0°$.

Figure 3: Top view of the fully-passive flapping-foil turbine prototype with the blade at two different positions during a given test in the water channel. The water is flowing from the bottom right corner of the figure toward the top left corner, which is perpendicular to the heaving motion. A video showing such a top view of the baseline case presented in Section 3.1 is available in the supplementary material provided with the online version of this paper.

channel floor was set to a very small gap of 5 mm, which corresponds to a tenth of the blade chord length. The blade span length (b) is 0.38 m and the water level was set to 0.42 m at rest. As a result, the blade is completely submerged during the tests, while all the other components are located above water, except for the end plates and a fraction of the shaft holding the blade. This can be seen in Fig. 4.

The fully-passive flapping-foil turbine prototype presented in this work was designed based on the optimal case reported by Veilleux and Dumas (2017). However, several aspects differ from their optimal 2D numerical case due to practical design limitations, especially regarding the Reynolds number, the static moment, the presence of Coulomb friction, the three-dimensionality of the flow, the blockage and the presence of a free surface. Besides, the prototype allows us to independently vary the three inertial properties, namely the heaving mass (m_h), the moment of inertia about the pitch axis (I_θ) and the static moment (S), as well as the heave damping ($D_{h,\mathrm{e}}$) and the heave and pitch stiffness coefficients (k_h and k_θ). More information about how these variations can be achieved is given in Appendix A.

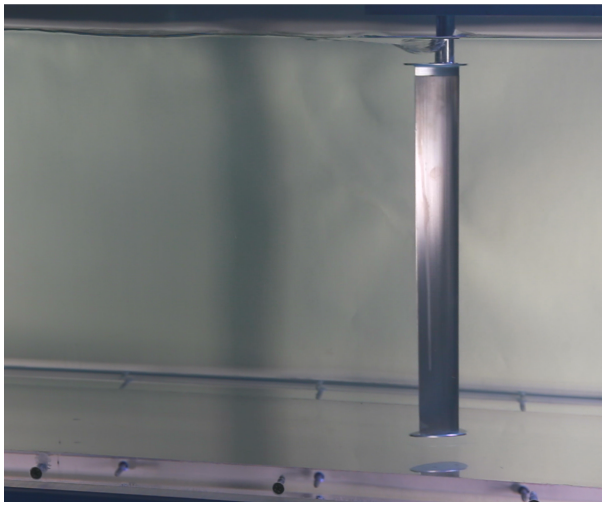

Figure 4: Side view showing the submerged turbine components, namely the blade, the end plates and a fraction of the shaft holding the blade. The water is flowing from right to left. A video showing such a side view of the baseline case presented in Section 3.1 is available in the supplementary material provided with the online version of this paper.

2.3. Measurement protocols

For each test, the blade is initially held in place at its equilibrium position, namely the middle of the channel in heave ($h/c = 0$) with the blade chord line being aligned with the inflow velocity ($\theta = 0$). The water velocity is then set to a desired value before suddenly releasing the blade. The blade positions in heave and in pitch are recorded at a sampling frequency of 83.3 Hz and during 120 seconds, which roughly corresponds to 100 oscillations of the blade, with two rotary encoders generating 10 000 pulses per revolution. The digital signals provided by each encoder are converted into analog signals (0-5 V) using a 14-bit digital-to-analog converter (DAC), and these analog signals are sampled with a NI USB-6218 data-acquisition board connected to a laptop.

In order to convert the reciprocating heaving motion into a rotational motion that can be measured by the heave encoder, a timing belt pulley is fixed to the shaft of the heave encoder and is in contact with a timing belt glued to an aluminum plate undergoing the heaving motion, as shown in Fig. 5. Note that the blade velocity components in heave and in pitch are computed using second-order central-difference schemes.

The inflow velocity (U_∞) is measured using Particle Image Velocimetry (PIV) on a vertical plane (xz) located 13 chord lengths upstream of the pitch axis and covering 0.8c in the streamwise (x) direction and 4.2c in the spanwise (z) direction. The PIV measurements are carried out with a sampling frequency of 100 Hz during 16 seconds, which roughly corresponds to between 15 and 20 blade cycles. The turbulent intensity of the inlet flow based on the streamwise velocity fluctuations is below 1% and the uniformity of the inflow has been verified by computing the standard deviations of the velocity profiles in the spanwise (z) and transverse (y) directions, which are around 0.1% in both directions.

Since the friction in the pitch and heave bearings can change over time due to their slight wear, it was estimated at the start and at the end of every series of experiments conducted in the channel. A range of values is therefore given to characterize the different friction contributions for a specific test. The methodology that has been used to estimate these friction contributions is presented in Appendix B.4.

The ambient temperature as well as the temperature of the aluminum sliding plate of the eddy-current brake are measured with a standard mercury thermometer and an infrared thermometer (Fluke 65), respectively. The ambient temperature during a given test is used to determine the water properties, namely its density and its dynamic viscosity, by interpolating the tabulated data available in the book of Munson et al. (2013). Regarding the temperature of the eddy-current brake's sliding plate, it is used to correct the values of the heave damping coefficient of the eddy-current brake, as described in Appendix B.4.

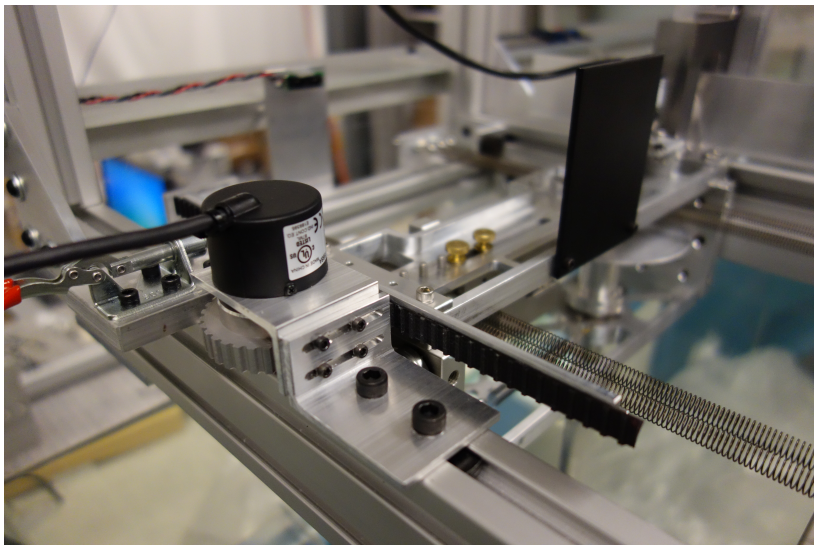

Figure 5: Timing belt used to convert the reciprocating heaving motion into a rotational motion for the heave encoder.

2.4. Performance metrics

The motions of the different cases considered are compared in terms of the reduced frequency (f^*), the phase lag between the heaving motion and the pitching motion (ϕ) and the amplitudes in heave (H_0^*) and in pitch (Θ_0). These metrics are defined as:

$$f_j^* = \frac{f_j\, c}{U_\infty}\,, \tag{5}$$

$$\phi_j = \frac{360}{T_j}\left(t_{\theta_{\max\, j}} - t_{h_{\max\, j}}\right) \quad \text{[degrees]}\,, \tag{6}$$

$$H_{0\,j}^* = \frac{h_{\max\, j} - h_{\min\, j}}{2c}\,, \tag{7}$$

$$\Theta_{0\,j} = \frac{\theta_{\max\, j} - \theta_{\min\, j}}{2}\,, \tag{8}$$

where the subscript j stands for the j$^{\text{th}}$ turbine blade oscillation, f is the frequency of the motions, which is always the same for both degrees of freedom for all the cases reported in this study, T is the oscillation period ($T = 1/f$), $h_{\max}$, $h_{\min}$, $\theta_{\max}$ and $\theta_{\min}$ are the extreme heave and pitch positions reached during a given turbine blade oscillation, and $t_{\theta_{\max}}$ and $t_{h_{\max}}$ are the instants at which these extreme positions are reached. Note that the value of ϕ obtained from Eq. 6 is given in degrees.

Two other metrics characterizing the energy extraction, namely the efficiency (η_{e}) and the power coefficient in heave ($\overline{C_{P_{h,\text{e}}}}$), both based on the cycle-averaged power dissipated in the eddy-current brake which models the energy extraction, are also used to compare the different cases that have been tested. They are defined as:

$$\eta_{\text{e}\,j} = \frac{\overline{P_{h,\text{e}\,j}}}{\dfrac{1}{2}\rho\, U_\infty^3\, b\, d_j}\,, \tag{9}$$

where:

$$\overline{P_{h,\text{e}\,j}} = \frac{1}{T_j}\int_t^{t+T_j}\left(D_{h,\text{e}}\,\dot{h}^2\right) dt\,, \tag{10}$$

and

$$\overline{C_{P_{h,e}\,j}} = \eta_{e\,j}\,\frac{d_j}{c}. \tag{11}$$

with b being the blade span length and d_j being the overall transverse extent of the blade motion during the j$^{\text{th}}$ turbine blade cycle (Kinsey and Dumas, 2008). In other words, d_j corresponds to the distance between the highest and the lowest points reached by any point on the blade surface during the j$^{\text{th}}$ cycle.

Note that these definitions of the efficiency and the power coefficient must not be confused with the definitions that are typically used for fully-constrained turbines (Kinsey and Dumas, 2014). Indeed, the efficiency and the power coefficient that are usually reported for fully-constrained turbine technology are based on the energy transferred from the flow to the turbine blade and do not take into account the power transmission efficiency. With the present experimental setup, it is not possible to directly compute the power transferred from the flow to the blade since the forces acting on the blade are not measured. The power dissipated in the heave damper that is used to compute η_e and $\overline{C_{P_{h,e}}}$ is necessarily smaller than the total power extracted from the flow because a fraction is inevitably lost due the undesired friction in the moving components.

Lastly, all the results presented in the following sections have been obtained by computing average values from 90 turbine blade cycles. For example:

$$f^* = \frac{1}{90}\sum_{j=1}^{90} f_j^* \ . \tag{12}$$

3. Results

3.1. Baseline case

Following a preliminary series of tests, a case achieving a high efficiency has been selected as the baseline case and is presented in this section. The parameters describing this baseline case as well as some metrics characterizing its performance are given in Table 2, while time evolutions of the pitch and heave positions are presented in Fig 6. Moreover, two videos of this case are available in the supplementary material provided with the online version of this paper.

Table 2: Baseline case description and performance.

Parameter	Value	Performance metric	Averaged value
Re	21 000	f^*	0.133 ± 0.001
m_h^*	3.36 ± 0.05	ϕ	99° ± 3°
I_θ^*	0.091 ± 0.001	H_0^*	0.891 ± 0.002
S^*	0.040 ± 0.001	Θ_0^*	85.0° ± 0.9°
$D_{h,\mathrm{e}}^*$	1.23 ± 0.03	η_e	26.8% ± 0.7%
k_h^*	1.91 ± 0.03	$\overline{C_{P_{h,e}}}$	0.68 ± 0.02
k_θ^*	0		
$D_{h,\mathrm{v}}^*$	[0.047 − 0.074] ± 0.008		
D_θ^*	[0.003 − 0.005] ± 0.003		
$C_{F_{y\,\mathrm{Coulomb}}}$	[0.07 − 0.07] ± 0.04		
$C_{M_{\mathrm{Coulomb}}}$	[0.015 − 0.021] ± 0.005		

It is worth recalling again that the amplitudes, the frequency and the phase lag between the heaving and the pitching motions are not constrained, but rather result from the structural and hydrodynamic parameters characterizing a specific case. It is therefore impressive to notice that the kinematics of the baseline case turn out to be very similar

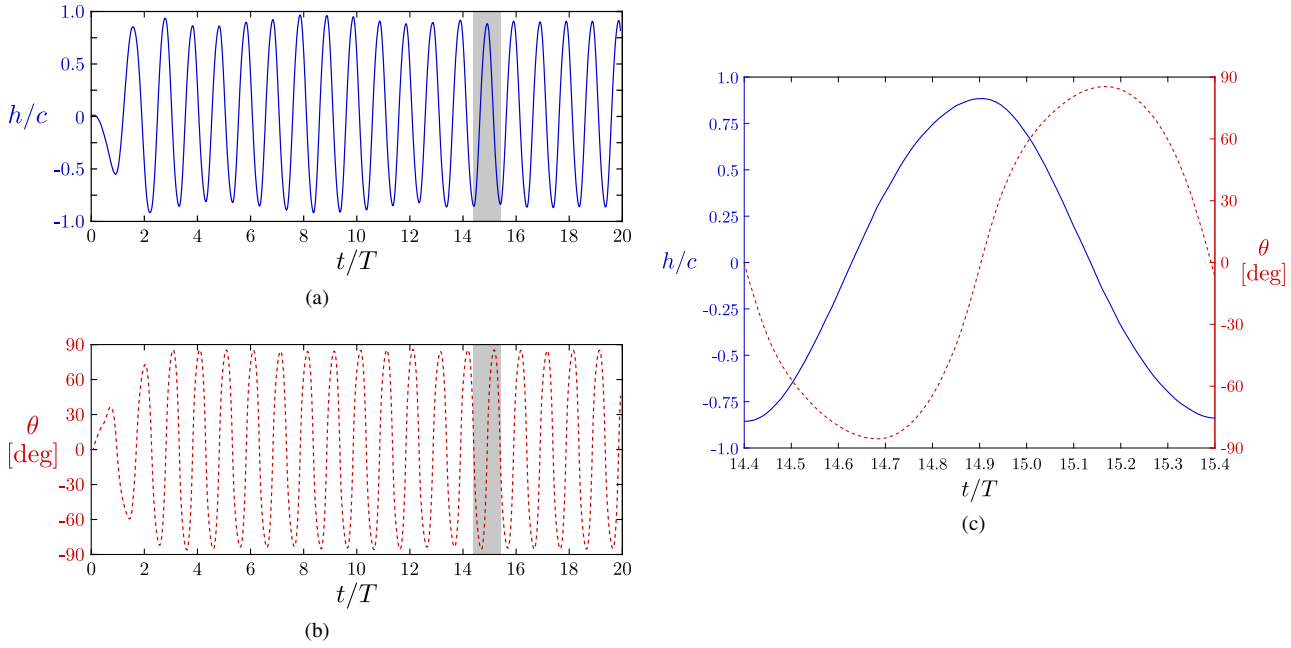

Figure 6: Heave (a) and pitch (b) positions over time for the baseline case (see Table 2), shown in solid blue and in dashed red respectively, with the blade released from its equilibrium position at $t/T = 0$, where t is the dimensional time and T is the dimensional oscillation period of the blade averaged over 90 oscillations. A zoom of the shaded area in (a) and (b), which approximately corresponds to one turbine blade oscillation, is shown in (c). The zoom area starts at an instant for which the pitch angle is zero and the heave position is close to a minimum.

to the motions leading to the best performance achieved with fully-constrained turbines. Indeed, previous studies devoted to the fully-constrained turbine concept have shown that high efficiencies are usually observed when the turbine blade undergoes large-amplitude motions in heave (on the order of one chord length) and in pitch ($\approx 80°$), at a reduced frequency between 0.10 and 0.20 approximately and with a phase lag close to 90° (Kinsey and Dumas, 2014; Young et al., 2014; Xiao and Zhu, 2014).

Following the 2D numerical works of Veilleux and Dumas (2017) and Wang et al. (2017), who respectively obtained efficiencies of 29.1% and 32% and power coefficients of 0.935 and 0.95, the current experimental work further demonstrates that such performance can be obtained despite the presence of some "real-life" effects such as the viscous and Coulomb friction contributions stemming from the bearings, the tip losses, the drag of the submerged fraction of the shaft holding the blade and the presence of a free surface. It is also interesting to note that since the undesired viscous damping in the heave bearings is about 5% of the eddy-current brake damping for the baseline case (see Table 2), the efficiency and the power coefficient would be both 5% larger if this undesired damping contribution was zero. An even larger increase would be expected if the viscous damping in pitch as well as the Coulomb friction in heave and in pitch could also be eliminated.

The regularity and the periodicity of the motions, once a permanent regime is reached, are notable. A quantitative measure of this periodicity is given in Table 3 by providing the standard deviations of the different performance metrics presented in Table 2. Considering that the ultimate objective of this study is to develop a simple and reliable energy extraction device, this makes the baseline case even more suitable for a turbine application.

It is interesting to note that the blade pitches passively even if $k^*_\theta = 0$ for the baseline case. By analyzing the relative contributions of each term appearing in the governing equations of motion (Eqs. 3 and 4), Veilleux and Dumas (2017) found that the dominant term responsible for limiting the pitch amplitude and reversing the pitch velocity for their optimal case was the hydrodynamic moment about the pitch axis for which a large peak was observed every half cycle. The contribution of the pitch spring stiffness, although not zero in their case, was negligible. Veilleux and Dumas (2017) have highlighted the fact that the large moment peak was related to the generation of a strong leading edge vortex following the deep stall of the blade. It was also responsible for a non-sinusoidal pitching motion with

Table 3: Averaged values and standard deviations of the performance metrics characterizing the baseline case computed from 90 blade cycles.

Performance metric	Averaged value	Standard deviation
f^*	0.133	0.014
ϕ	99°	3°
H_0^*	0.891	0.017
Θ_0^*	85.0°	0.5°
η_e	26.8%	0.6%
$\overline{C_{P_{h,e}}}$	0.68	0.02

smaller pitch velocities observed when the blade is approaching an extremum in pitch than when the blade departs from an extremum.

Unfortunately, the experimental setup used for the current study does not allow measuring the hydrodynamic forces and moment acting on the blade, hence preventing us from performing a similar analysis. However, PIV measurements have been carried out and a series of instantaneous vorticity fields around the blade are presented in Fig. 7. This figure shows that the blade is subject to deep stall and that a large leading edge vortex is shed every half cycle in the case of the baseline operating point, as for the optimal case of Veilleux and Dumas (2017). Furthermore, a similar non-sinusoidal pitching motion has been obtained in the current study, as shown in Fig. 6c. Considering that the flow fields and the time evolutions of the pitch angle are very similar in both studies and that the contribution of the pitch spring is close or equal to zero in both cases, the hydrodynamic moment is most likely responsible for limiting the pitch amplitude and reversing the pitch velocity for the baseline case of the current study, as it was for the optimal case found by Veilleux and Dumas (2017).

Even if the moment about the pitch axis cannot be directly measured, all the terms on the right hand side of Eq. 4 can be computed, which allows estimating the moment coefficient by summing all of them. The evolution of the terms appearing in Eq. 4 are shown in Fig. 8 over the same time span as in Fig. 6c, which approximately corresponds to one complete blade cycle starting when the pitch angle is zero and the heave position is close to a minimum. The results show that the inertia term ($I_\theta^* \ddot{\theta}^*$) is much larger than all the other terms appearing on the right hand side of Eq. 4. This confirms the hypothesis that the pitching motion of the baseline case essentially results from the balance between the moment generated by the fluid flow and the inertia term. By observing Figs. 6c, 7 and 8, one can notice that the large leading edge vortex that is generated as the blade stalls results in a large positive moment peak when $\theta < 0$ (see the instants $t/T = 0.4$ in Fig. 7 and $t/T \approx 14.8$ in Fig. 8), which in turn results in a large positive pitch acceleration that limits the pitch amplitude. Once the leading edge vortex is shed beyond the trailing edge, the moment quickly becomes negative (see the instants $t/T = 0.5$ in Fig. 7 and $t/T \approx 14.9$ in Fig. 8). A similar behavior was observed by Veilleux and Dumas (2017) and is described in more details in their work. Note that the results presented in Fig. 8 are a bit noisy because they involve the computation of the heave and pitch accelerations from the position measurements. In order to limit the uncertainty of the results presented in this figure, the sampling rate was reduced to half its nominal value of 83.3 Hz, used for the rest of the current study, to 41.7 Hz. This results in an uncertainty of the inertia term corresponding to 5% of its peak value.

A static instability, known as divergence, can occur when the restoring moment stemming from the pitch springs is not large enough to counteract the hydrodynamic moment (Dowell, 2004). More precisely, the theory predicts that the critical dimensionless pitch spring stiffness coefficient ($k^*_{\theta\,\mathrm{crit}}$) is given by:

$$k^*_{\theta\,\mathrm{crit}} = \frac{\pi\, e}{c}\,, \tag{13}$$

where e is the distance between the point of application of the fluid force and the pitch axis and it is defined positive when the point of application of the fluid force is located upstream of the pitch axis. The blade is unstable when $k^*_\theta < k^*_{\theta\,\mathrm{crit}}$, which means that this instability can only occur if the pitch axis is located downstream of the point at which the fluid force acts.

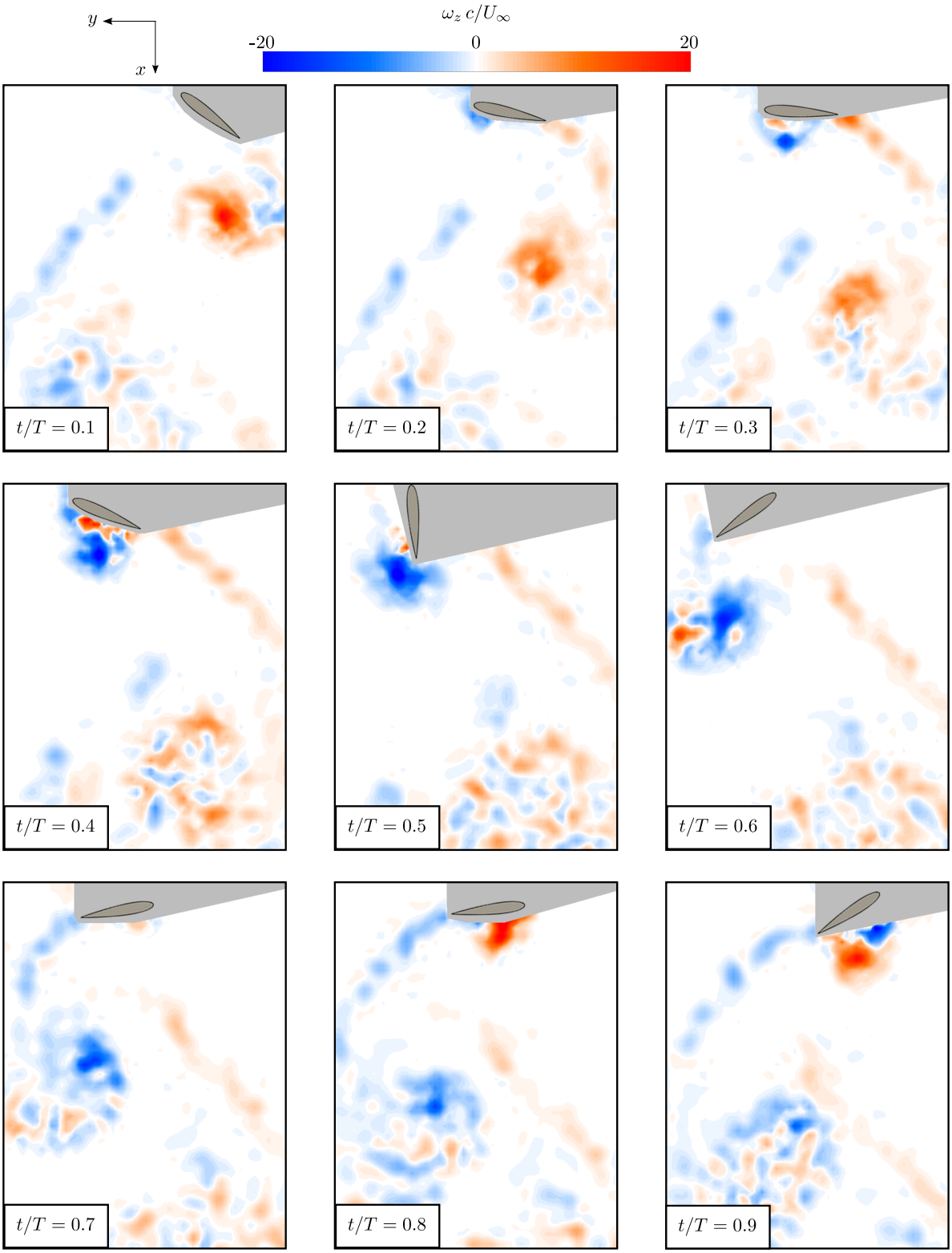

Figure 7: Snapshots of the normalized spanwise vorticity field measured by PIV at different instants during one representative blade cycle of the baseline case. The start of the cycle ($t/T = 0$) is defined as an instant for which the pitch angle is zero and the heave position is close to a minimum. As a result, the time $t/T = 0$ in this figure is similar to the time $t/T = 14.4$ in Figs. 6 and 8.

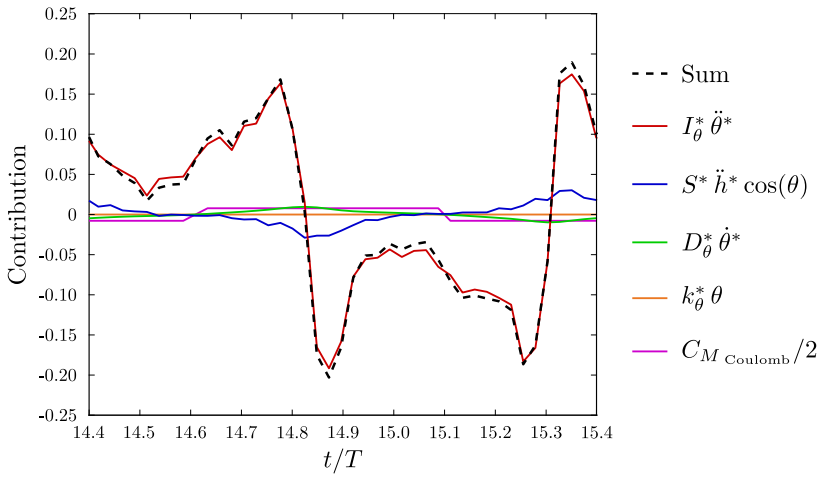

Figure 8: Time evolutions of the terms on the right hand side of Eq. 4 for the baseline case over the same time span as in Fig. 6c, i.e., approximately one turbine cycle. The sum of all the terms (dashed black line) estimates $C_M/2$.

Based on the linear unsteady theory (Dowell, 2004; Fung, 2008) and considering a thin symmetric foil, the fluid force is expected to act around the quarter-chord point. Since the pitch axis is located further downstream, at the third-chord point, and because $k^*_\theta = 0$, the baseline case of the current study is expected to be subject to the divergence instability. The fact that the blade starts to pitch even when it is being held in place in the heave direction supports this inference. Indeed, this pitching motion would not occur if the present turbine was rather driven by the classical flutter instability, which is a coupled-mode instability that requires both degrees of freedom to be active in order to arise. Moreover, the motions of the current turbine are always damped when using pitch springs with too large stiffness coefficients, as shown in Section 3.2.4, which again suggests that the divergence instability is the driving mechanism of this fully-passive flapping-foil prototype. The occurrence of this static instability can also explain why the transient period following the release of the blade is so short, as observed in Figs. 6a and 6b. About only two oscillation periods ($t/T \approx 2$) are required before the turbine reaches a permanent regime characterized by stable limit-cycle oscillations (LCO) of large amplitudes. It is important to note that the theory leading to the divergence instability threshold, given by Eq. 13, relies on the assumption of small displacements and a quasi-static approximation. According to this theory, nothing limits the growth of the pitch amplitude when the blade is unstable. This theory is therefore useful to explain why the pitching motion is initiated, which in turn drives the heaving motion, but it does not apply when large amplitudes are reached in heave and in pitch because the nonlinearities of the flow become important.

By releasing the turbine blade from different initial pitch angles, it has been found that the permanent response of the baseline case is not affected by variations of the initial conditions. Moreover, tests consisting of temporary increasing or decreasing the flow velocity above or below its nominal value were conducted while the blade was oscillating in the water. The turbine response was always returning to the same permanent regime following these perturbations. These observations corroborate the findings of Peng and Zhu (2009), Amandolese et al. (2013) and Wang et al. (2017) for large-amplitude and periodic limit-cycle oscillations. These studies also showed that, for other types of responses, an oscillating blade could be significantly sensitive to the initial conditions and could be subject to hysteresis, but this has not been observed during the current study.

3.2. Sensitivity of the turbine performance to the governing structural parameters

In this section, the impact of various structural parameters affecting the turbine blade dynamics is analyzed. The effects of each structural parameter are investigated individually by keeping all the other structural parameters constant with their baseline value (see Table 2).

Unless otherwise specified, all the tests presented in this section were conducted with an inflow velocity of 0.38 m/s, which corresponds to a Reynolds number of 21 000 based on the chord length. Moreover, all the cases that are presented are similar to the baseline case in terms of the low sensitivity to the initial conditions and to perturbations, the regularity of the permanent response and the shortness of the initial transient period.

In the figures presented in the following sections, empty markers are used to identify the baseline case and to discriminate it from the other cases (filled markers). For the sake of clarity, the uncertainties are not shown in the figures, but they are available in the supplementary material provided with the online version of this paper.

In order to evaluate the repeatability of the results, some experiments have been carried out twice for a given set of structural parameters. More specifically, the same set of parameters was tested before and after each series of experiments. The values obtained from these tests are included in Figs. 9, 11, 13, 14 and 15. This explains why two markers can be observed for one specific value of the structural parameter considered. The baseline parameter values were used to conduct these repeatability tests except when studying the effects of k_θ^* and U_∞, for which $k_\theta^* = 0.068$ and $U_\infty = 0.35$ m/s were respectively used instead.

3.2.1. Heave stiffness

Fig. 9 shows the impact of the dimensionless heave stiffness (k_h^*) on various performance metrics. All the other structural parameters are kept constant except for the heaving mass (m_h^*), which slightly varies between the various cases because of the different number of heave springs used for each of them, as indicated in the legend of Fig. 9.

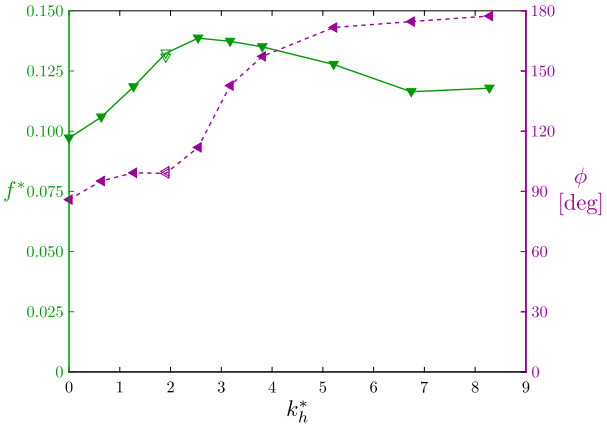

(a) Reduced frequency (solid green) and phase lag between the heaving and the pitching motions (dashed purple)

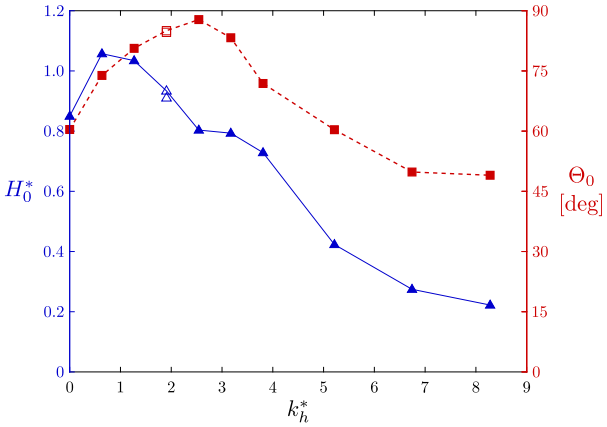

(b) Heave amplitude (solid blue) and pitching amplitude (dashed red)

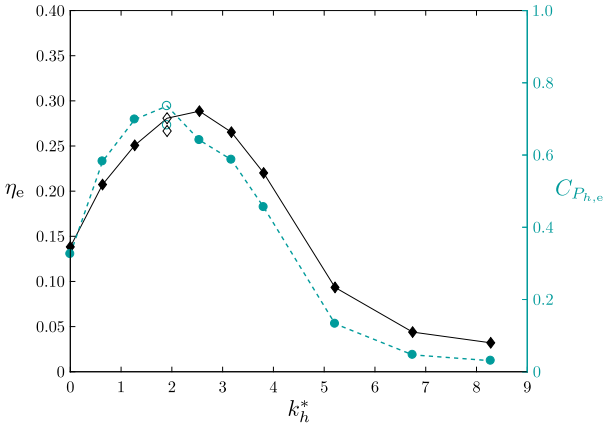

(c) Efficiency (solid black) and power coefficient (dashed turquoise)

Figure 9: Various performance metrics as functions of the dimensionless heave stiffness (k_h^*). Empty markers are used to identify the baseline case and the uncertainties are provided in the supplementary material along with the tabulated data used to produce this figure. $m_h^* = [3.34 - 3.38]$; $I_\theta^* = 0.091$; $S^* = 0.040$; $D_{h,e}^* = 1.21$; $k_\theta^* = 0$; $D_{h,v}^* = [0.047 - 0.074]$; $D_\theta^* = [0.003 - 0.005]$; $C_{F_y\,\text{Coulomb}} = [0.07 - 0.07]$; $C_{M\,\text{Coulomb}} = [0.015 - 0.021]$.

The maximum efficiency, reduced frequency and pitch amplitude, namely 28.9%, 0.139 and 87.8°, are all observed

at the same operating point: $k_h^* = 2.54$. While the efficiency and the power coefficient follow the same trend, the largest power coefficient, with a value of 0.74, is obtained for a slightly smaller dimensionless heave stiffness ($k_h^* = 1.91$). This can be explained by the fact that the heave amplitude is larger with $k_h^* = 1.91$ than with $k_h^* = 2.54$, hence allowing for more energy extraction. However, the efficiency decreases from $k_h^* = 2.54$ to $k_h^* = 1.91$ because the kinetic energy flux passing through the turbine extraction plane increases even more than the power extracted.

Another noteworthy observation is that large amplitude motions with a significant energy extraction are even observed with no spring in heave and no spring in pitch (zero stiffness). The adequate synchronization between the pitching and the heaving motions leading to a good performance for this case, although not optimal, is therefore mainly due to the hydrodynamic force and moment acting on the turbine blade. This has indeed been shown by Veilleux (2014) who analyzed in more details a similar case with no spring in heave and no spring in pitch.

Furthermore, it is found that the pitch and heave amplitudes, the efficiency and the power coefficient all quickly drop when k_h^* exceeds approximately 3. This drop is related to the sudden transition from a phase lag around 90° between the heaving motion and the pitching motion to a phase lag close to 180°. Indeed, it is known that a phase lag of 90° is close to optimal when the pitch axis is located at the third-chord point (Xiao and Zhu, 2014) because the largest force acting on the blade in the heave direction and the largest heave velocity occur approximately at the same time in this case. Conversely, the force component in the heave direction is completely out of phase with the heave velocity when the phase lag is 180°.

While the phase lag between the heaving and the pitching motions is considerably altered as the dimensionless heave stiffness is increased, the reduced frequency is not affected as much. Moreover, the reduced frequency is neither directly correlated with the heave natural frequency ($f_{n,h}^* = \sqrt{k_h^*/m_h^*}/2\pi$), as shown in Fig. 10, nor with the pitch natural frequency ($f_{n,\theta}^* = \sqrt{k_\theta^*/I_\theta^*}/2\pi$) since no pitch springs are used for all the cases presented in Figs. 9 and 10, resulting in $f_{n,\theta}^* = 0$. This suggests that the reduced frequency is related to another time scale associated to the fluid flow around the turbine blade. However, the heave natural frequency remains relevant since it is found that the point of maximum efficiency and maximum pitch amplitude are obtained when the reduced frequency and the heave natural frequency coincide, which occurs when $k_h^* = 2.54$. Furthermore, Fig. 10 shows that the reduced frequency increases with the heave natural frequency until they coincide and then decreases as the heave natural frequency further increases. It is also worthwhile to mention that the abrupt transition of the phase lag from 90° to 180° occurs when the heave natural frequency becomes larger than the reduced frequency.

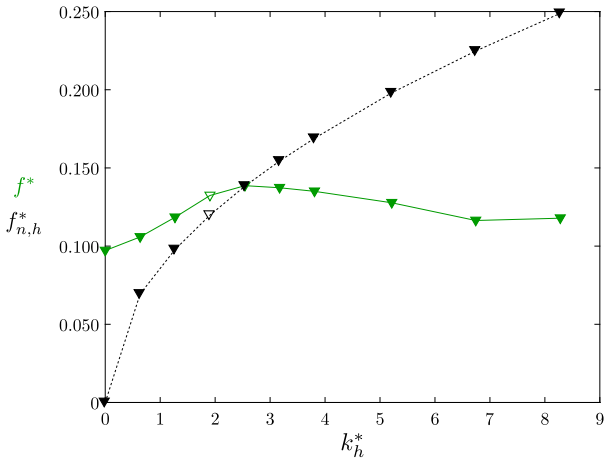

Figure 10: Comparison of the reduced frequency (f^* in solid green) and the reduced heave natural frequency ($f_{n,h}^*$ in dashed black) as a function of the dimensionless heave stiffness (k_h^*). Empty markers are used to identify the baseline case.

3.2.2. Heaving mass

The effect of the dimensionless heaving mass is presented in Fig. 11. Due to the experimental setup limitations, it is not possible to vary the dimensionless heaving mass to the same extent than the dimensionless heave stiffness. It is

therefore normal to observe smaller variations for the different performance metrics in Fig. 11 than what is observed in Fig. 9.

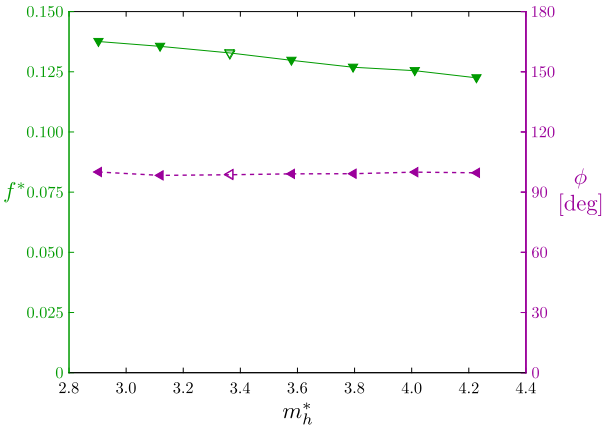

(a) Reduced frequency (solid green) and phase lag between the heaving and the pitching motions (dashed purple)

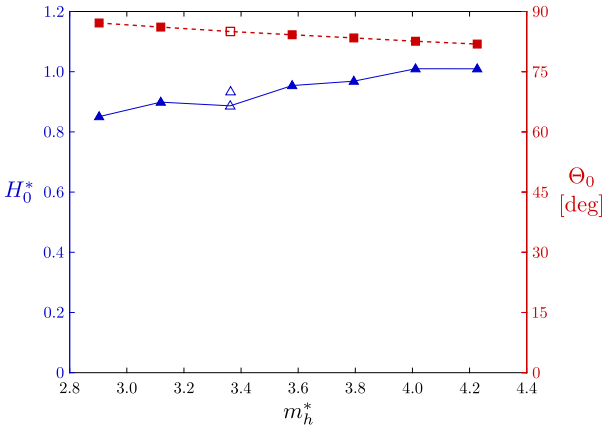

(b) Heave amplitude (solid blue) and pitching amplitude (dashed red)

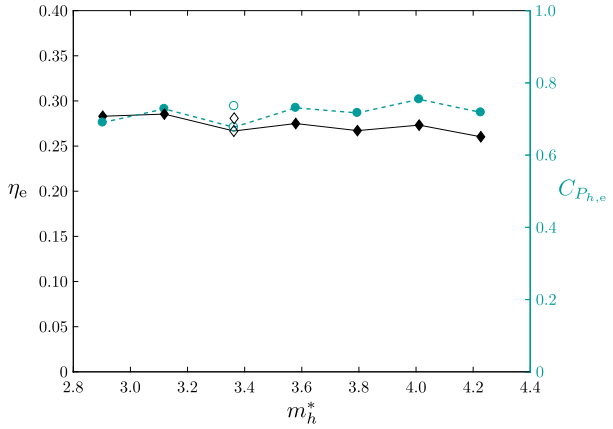

(c) Efficiency (solid black) and power coefficient (dashed turquoise)

Figure 11: Various performance metrics as functions of the dimensionless heaving mass (m_h^*). Empty markers are used to identify the baseline case and the uncertainties are provided in the supplementary material along with the tabulated data used to produce this figure. $I_\theta^* = 0.091$; $S^* = 0.040$; $D_{h,\mathrm{e}}^* = 1.21$; $k_h^* = 1.91$; $k_\theta^* = 0$; $D_{h,\mathrm{v}}^* = [0.047 - 0.074]$; $D_\theta^* = [0.003 - 0.005]$; $C_{F_{y\,\mathrm{Coulomb}}} = [0.07 - 0.07]$; $C_{M_{\,\mathrm{Coulomb}}} = [0.015 - 0.021]$.

It is found that increasing the dimensionless heaving mass by 45% from the minimum value tested only results in a variation of 2.5% (absolute) in terms of the efficiency (see Fig. 11c). This means that the manufacturer of a similar fully-passive flapping-foil turbine would have some useful freedom regarding this structural parameter, which should greatly facilitate the design process. Regarding the power coefficient, it is even less affected than the efficiency by variations of the heaving mass, as was also observed by Deng et al. (2015) in the case of a flapping-foil turbine with a prescribed pitching motion and an elastically-supported heaving motion.

The good performances reported here over the entire range of dimensionless heaving masses that have been tested is related to the fact that the phase lag between the heaving and the pitching motions remains close to the optimal value of 90°. In the previous section, it was shown that the phase lag was shifting toward 180° as the heave natural frequency was exceeding the reduced frequency. Figure 12 shows that the heave natural frequency remains below the reduced frequency when varying the dimensionless heaving mass. It is expected that the heave natural frequency would exceed the reduced frequency with smaller dimensionless heaving mass and that the phase lag would then tend toward 180°, as is observed when increasing the dimensionless heave stiffness (see Figs. 9a and 10). As mentioned earlier, it is

unfortunately not possible to test smaller values of dimensionless heaving mass with the current experimental setup.

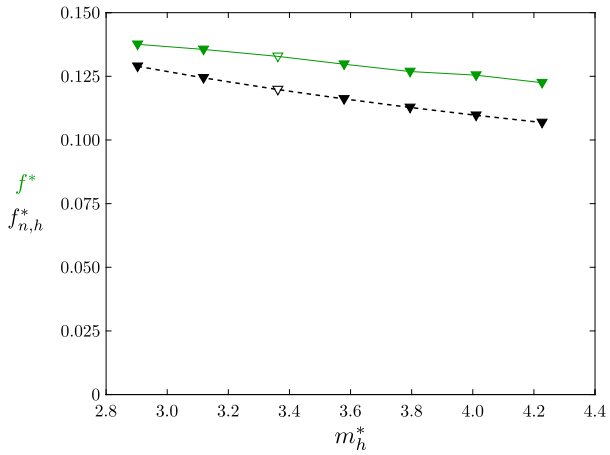

Figure 12: Comparison of the reduced frequency (f^* in solid green) and the reduced heave natural frequency ($f^*_{n,h}$ in dashed black) as a function of the dimensionless heaving mass (m^*_h). Empty markers are used to identify the baseline case.

It can be observed in Figs. 9 and 11 that the dimensionless heave stiffness and the dimensionless heaving mass have opposite effects on the motions around the baseline case. Indeed, Fig. 9 shows that, around the baseline dimensionless heave stiffness coefficient ($k^*_h = 1.91$), the reduced frequency and the pitch amplitude increase while the heave amplitude decreases as the dimensionless heave stiffness is increased. The opposite behavior is observed in Fig. 11 for increasing values of the dimensionless heaving mass. This is because the heaving motion is very close to a sine wave for all the cases presented in Figs. 9 and 11. Consequently, the heave acceleration is also resembling a sine wave, but in antiphase with the heave position. In other words, the inertia term ($m^*_h \ddot{h}^*$) and the stiffness term ($k^*_h h^*$), appearing in Eq. 3, have similar shapes as functions of time, but with opposite signs.

3.2.3. Heave damping

For the sake of conciseness, the term dimensionless heave damping is used in this section to refer to the dimensionless heave damping stemming only from the eddy-current brake ($D^*_{h,\mathrm{e}}$). The viscous damping contribution coming from the bearings is therefore not included in the analysis. The reader is referred to Appendix B.4 for more details about the evaluation of the heave damping. Let us recall that the energy dissipated in the eddy-current brake represents the energy extracted from the flow that could be converted into electricity by an electric generator.

Fig. 13 presents the various performance metrics considered as functions of the dimensionless heave damping. It is found that increasing the dimensionless heave damping does not significantly affect the reduced frequency and the phase lag between the heaving and the pitching motions, but it results in a considerable decrease of the heave amplitude, and, to a lesser extent, of the pitch amplitude. In spite of these amplitude decreases, Fig. 13c shows that the efficiency remains relatively constant over the range of dimensionless heave damping coefficients that have been tested. However, because of this constant efficiency and the decreasing amplitudes, the power coefficient decreases when increasing the damping. These observations are very relevant in practice as they suggest that varying the dimensionless heave damping allows controlling the turbine blade amplitudes in heave and in pitch without affecting the efficiency too much. This could be especially useful when such turbines are deployed in an environment restricted in space or if several turbines are positioned in close proximity.

3.2.4. Pitch stiffness

A very different behavior is observed when increasing the dimensionless pitch stiffness. Indeed, Fig. 14 shows that the motions are completely damped when $k^*_\theta = 0.154$ or $k^*_\theta = 0.236$. For these two cases, the blade is always returning to its equilibrium position, both in heave and in pitch, even if large heave positions and pitch angles are used as the initial condition. As mentioned in Sec. 3.1, this supports the hypothesis that the blade is subject to the

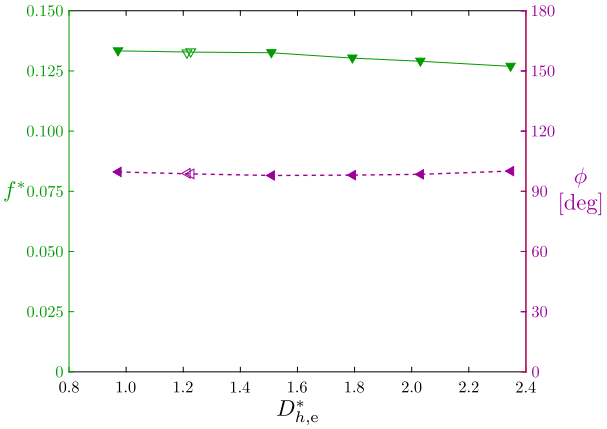

(a) Reduced frequency (solid green) and phase lag between the heaving and the pitching motions (dashed purple)

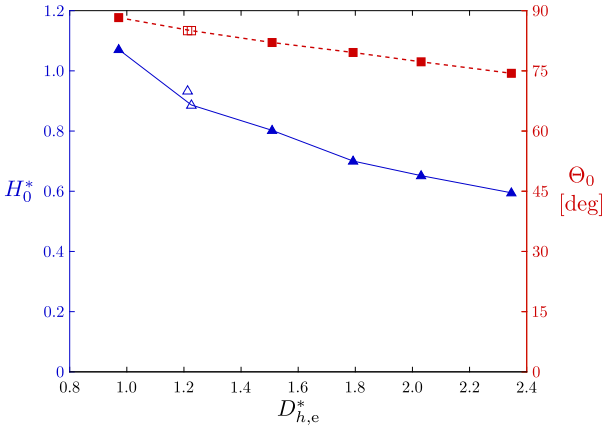

(b) Heave amplitude (solid blue) and pitching amplitude (dashed red)

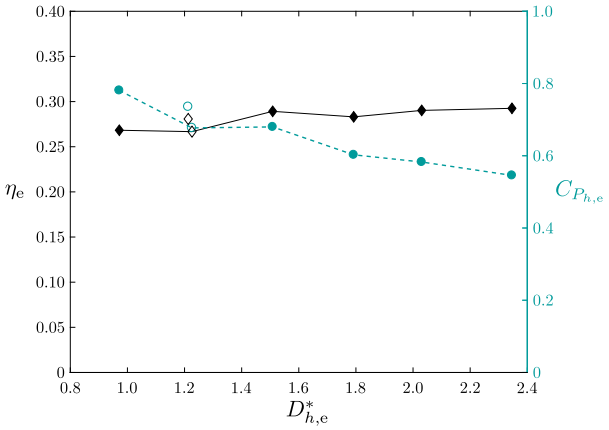

(c) Efficiency (solid black) and power coefficient (dashed turquoise)

Figure 13: Various performance metrics as functions of the dimensionless eddy-current brake damping in heave ($D^*_{h,\mathrm{e}}$). Empty markers are used to identify the baseline case and the uncertainties are provided in the supplementary material along with the tabulated data used to produce this figure. $m^*_h = 3.36$; $I^*_\theta = 0.091$; $S^* = 0.040$; $k^*_h = 1.91$; $k^*_\theta = 0$; $D^*_{h,\mathrm{v}} = [0.047 - 0.074]$; $D^*_\theta = [0.003 - 0.005]$; $C_{F_{y\,\mathrm{Coulomb}}} = [0.07 - 0.07]$; $C_{M\,\mathrm{Coulomb}} = [0.015 - 0.021]$.

divergence instability, which only occurs when the dimensionless pitch stiffness coefficient is below a given threshold (see Eq. 13).

Fig. 14 also shows that both the efficiency and the power coefficient could increase for non-zero dimensionless pitch stiffness compared to the baseline case, for which the dimensionless pitch stiffness is zero (no pitch springs). Indeed, the maximum efficiency and power coefficient values that have been observed throughout this experimental campaign, namely 31.0% and 0.86, have been obtained with $k^*_\theta = 0.051$. This is the operation point at which the reduced frequency and the pitch natural frequency are the closest to each other, with a difference of about 5% between them. Once again, this good performance is related to the fact that the phase lag between the heaving and the pitching motions is close to the optimal value of 90°. It is worth mentioning that this high efficiency is obtained even if the pitch amplitude considerably decreases when using non-zero dimensionless pitch stiffness coefficients.

Lastly, it is found that the reduced frequency does not follow the trend of the pitch natural frequency, as it decreases for increasing pitch stiffness coefficients. This suggests once again that the reduced frequency of the passive motions is related to a time scale of the fluid flow around the blade, as mentioned in Section 3.2.1.

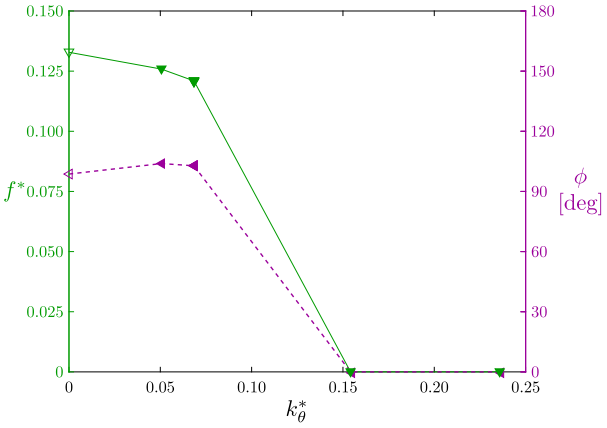

(a) Reduced frequency (solid green) and phase lag between the heaving and the pitching motions (dashed purple)

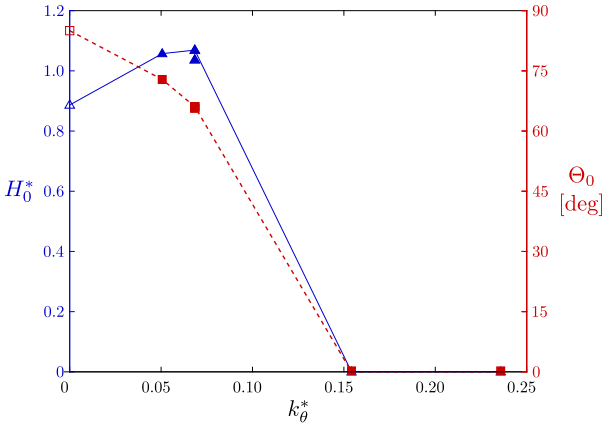

(b) Heave amplitude (solid blue) and pitching amplitude (dashed red)

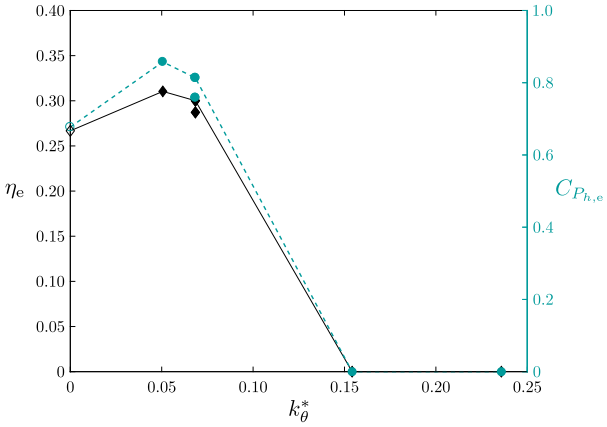

(c) Efficiency (solid black) and power coefficient (dashed turquoise)

Figure 14: Various performance metrics as functions of the dimensionless pitch stiffness (k_θ^*). Empty markers are used to identify the baseline case and the uncertainties are provided in the supplementary material along with the tabulated data used to produce this figure. $m_h^* = 3.36$; $I_\theta^* = 0.091$; $S^* = 0.040$; $D_{h,\mathrm{e}}^* = 1.21$; $k_h^* = 1.91$; $D_{h,\mathrm{v}}^* = [0.069 - 0.070]$; $D_\theta^* = [0.002 - 0.002]$; $C_{F_{y\,\mathrm{Coulomb}}} = [0.04 - 0.06]$; $C_{M_{\,\mathrm{Coulomb}}} = [0.02 - 0.02]$.

3.2.5. Moment of inertia and static moment

The turbine prototype used for the current study allows testing only two different values of the moment of inertia (I_θ) and three different values of the static moment (S). Moreover, with the current turbine design, it is not possible to modify these parameters without slightly affecting the heaving mass, as described in Appendix A.2. Indeed, the heaving mass is increased by 4% compared to the baseline case when I_θ or S are varied. Nevertheless, all the tests conducted to assess the effects of the static moment are characterized with this same increased mass value.

The performance metrics of the different cases that have been tested are given in Tables 4 and 5. One can notice that the variations of both the moment of inertia and the static moment do not significantly affect the turbine permanent response. In the case of the dimensionless static moment, it is found that a larger value results in slightly smaller pitch amplitudes, efficiencies and power coefficients. In future works, it would be useful to extend the range covered by these two parameters to better evaluate their full impact.

3.3. Effect of the inflow velocity on the turbine performance

So far, the effects of varying different dimensionless structural parameters have been presented. These different cases correspond to different designs of the fully-passive flapping-foil concept. In this section, we turn our attention

Table 4: Various performance metrics as functions of the dimensionless moment of inertia about the pitch axis (I_θ^*). The uncertainties are provided in the supplementary material. $S^* = 0.040$; $D_{h,\mathrm{e}}^* = 1.21$; $k_h^* = 1.91$; $k_\theta^* = 0$; $D_{h,\mathrm{v}}^* = [0.047 - 0.074]$; $D_\theta^* = [0.003 - 0.005]$; $C_{F_y\,\mathrm{Coulomb}} = [0.07 - 0.07]$; $C_{M\,\mathrm{Coulomb}} = [0.015 - 0.021]$.

I_θ^*	m_h^*	f^*	ϕ [deg]	H_0^*	Θ_0^*	η_e	$\overline{C_{P_{h,\mathrm{e}}}}$
0.091	$m_h^* = 3.36$	0.131	100	0.911	84.6	26.7%	0.68
0.117	$m_h^* = 3.50$	0.131	97	0.908	87.3	26.5%	0.68

Table 5: Various performance metrics as functions of the dimensionless static moment (S^*). The uncertainties are provided in the supplementary material. $m_h^* = 3.50$; $I_\theta^* = 0.117$; $D_{h,\mathrm{e}}^* = 1.21$; $k_h^* = 1.91$; $k_\theta^* = 0$; $D_{h,\mathrm{v}}^* = [0.047 - 0.074]$; $D_\theta^* = [0.003 - 0.005]$; $C_{F_y\,\mathrm{Coulomb}} = [0.07 - 0.07]$; $C_{M\,\mathrm{Coulomb}} = [0.015 - 0.021]$.

S^*	f^*	ϕ [deg]	H_0^*	Θ_0^*	η_e	$\overline{C_{P_{h,\mathrm{e}}}}$
0.023	0.128	99	0.935	86.8	27.3%	0.70
0.040	0.131	97	0.908	87.3	26.5%	0.68
0.056	0.132	95	0.864	87.8	25.1%	0.63

to the effects of varying the inflow velocity (U_∞) for a given set of dimensional structural parameters. Consequently, some dimensionless structural parameters do not remain constant since they vary with U_∞ (see their definitions in Section 2.1). Fig. 15 therefore provides some information about the response of a specific turbine design, with fixed structural parameters, to different inflow velocities.

It is found that the phase lag is not significantly altered when the inflow velocity varies from approximately 0.35 m/s to 0.62 m/s. As a result, large efficiencies and power coefficients are still obtained for all the inflow velocities that have been tested. Even though the efficiency decreases slightly when increasing the inflow velocity, the power coefficient remains relatively constant because of the considerable increase of the heave amplitude. This is a significant finding as this means that the power output that could be converted into electricity by this specific turbine design would not be much affected by the velocity perturbations that could occur in the river or the tidal current in which this turbine would be deployed.

4. Conclusion

A fully-passive flapping-foil turbine prototype has been successfully designed and tested in a water channel. This innovative concept may lead to significant simplifications of some previously tested flapping-foil turbine designs, which should yield cheaper and more reliable devices. Large-amplitude periodic motions have been observed and these self-induced and self-sustained motions have led to a very good performance in terms of the efficiency and the power coefficient, which have respectively reached 31.0% and 0.86. The present experimental demonstration therefore confirms the feasibility and the great potential of the fully-passive concept.

Seven structural and inflow parameters have been independently varied around a baseline case. Good performances have been achieved over a large range of parameter values, which is important in practice since this gives some flexibility to the designer of such turbines. Periodic motions of large amplitudes leading to a high efficiency have even been observed with no pitch spring and no heave spring. The phase lag between the heaving and the pitching motions has been found to be a critical factor and it appears to be related to the ratio between the reduced frequency of the turbine blade motions and the heave natural frequency. Moreover, the current results have shown that no sustained motions could be obtained when the dimensionless pitch stiffness coefficient is larger than $k_\theta^* = 0.154$. This is because the divergence instability is believed to be the driving mechanism of the current fully-passive flapping-foil turbine prototype. Consequently, the position of the pitch axis is expected to play a significant role as it is a crucial parameter

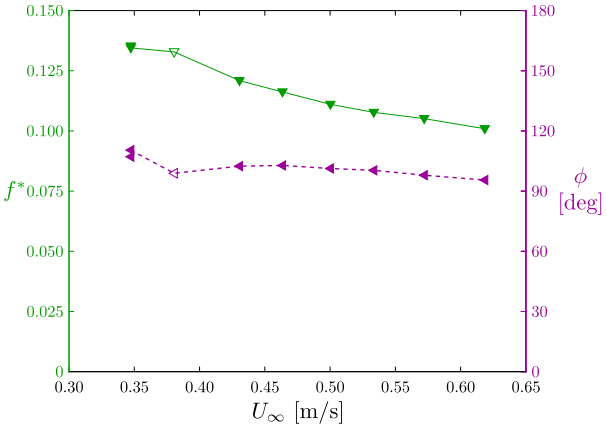

(a) Reduced frequency (solid green) and phase lag between the heaving and the pitching motions (dashed purple)

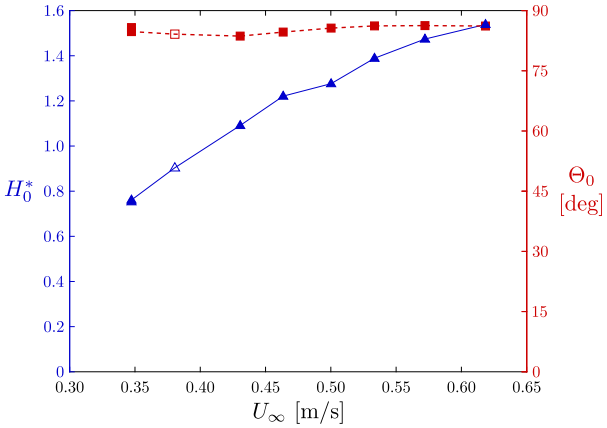

(b) Heave amplitude (solid blue) and pitching amplitude (dashed red)

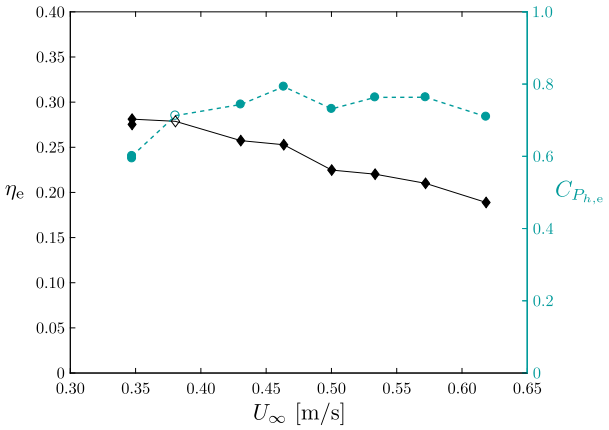

(c) Efficiency (solid black) and power coefficient (dashed turquoise)

Figure 15: Various performance metrics as functions of the inflow velocity (U_∞). Empty markers are used to identify the baseline case and the uncertainties are provided in the supplementary material along with the tabulated data used to produce this figure. $m_h^* = 3.36$; $I_\theta^* = 0.091$; $S^* = 0.040$; $D_{h,e}^* = 1.21$; $k_h^* = 1.91$; $k_\theta^* = 0$; $D_{h,v}^* = [0.063 - 0.072]$; $D_\theta^* = [0.003 - 0.007]$; $C_{F_{y\,\mathrm{Coulomb}}} = [0.04 - 0.05]$; $C_{M_{\,\mathrm{Coulomb}}} = [0.01 - 0.01]$; Re = 21 000 at $U_\infty = 0.38$ m/s (baseline case).

for the divergence instability (Dowell, 2004; Fung, 2008). This particular aspect should be investigated in futures studies along with the effects of the tip losses.

5. Acknowledgements

Financial support from the Natural Sciences and Engineering Research Council of Canada (NSERC Discovery Grant/RGPIN/121819-2013 and CGS-D scholarship), the Tyler Lewis Clean Energy Research Foundation (2016 TL-CERF grant) and the Leadership and Sustainable Development Scholarship Program of Université Laval is gratefully acknowledged by the authors. The authors also wish to thank Marc-André Plourde Campagna, Sylvain Ménard, Yves Jean and Thierry Villeneuve for their help regarding the design and fabrication of the turbine prototype.

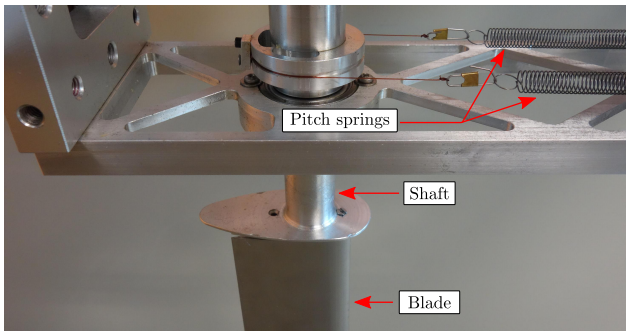

Figure A.1: Pitch springs attached to the shaft holding the turbine blade.

Appendix A. Structural parameters

Appendix A.1. Elastic supports

The heaving carriage is attached to the fixed structure of the turbine with extension springs. Two different sets of extension springs can be used and the number of springs attached to the carriage can also be varied from zero spring to a maximum of 6 pairs of springs (12 springs; see Fig. 3 where 3 pairs of springs can be seen). In pitch, the number of springs that can be used is limited to either zero or two, but springs with four different stiffness coefficients have been tested. Note that the desired torsional stiffness is obtained through the use of extension springs with one of their end fixed to the carriage and the other end attached to a cable which is fastened to the shaft holding the blade, thereby undergoing the pitching motion, as shown in Fig. A.1. Both the heave springs and the pitch springs can be seen in Fig. 3.

As mentioned earlier, a linear damper is used as an energy sink in heave. It consists of a thin aluminum sliding plate which is undergoing the heaving motion and passing, without making contact, between two magnets yoked together with 1020 carbon steel to form an eddy-current brake. This eddy-current brake is shown in Fig. A.2 and a schematic is presented in Fig. A.3. This damper is similar in principle to the one that has been used by Abiru and Yoshitake (2011, 2012) for their flapping-foil turbine with a prescribed pitching motion and a passive heaving motion or by Pigolotti et al. (2017) for their fully-passive flapping-plate setup.

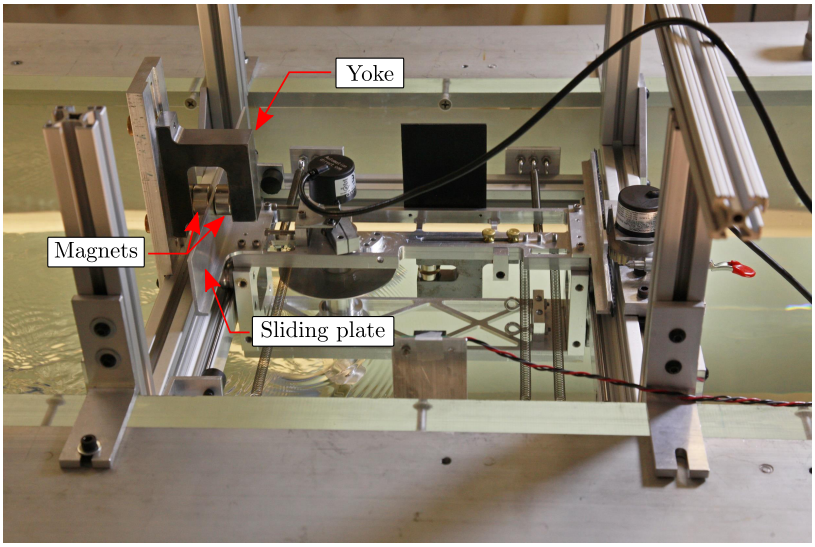

Figure A.2: Eddy-current brake used as the heave damper which provides the desired energy sink.

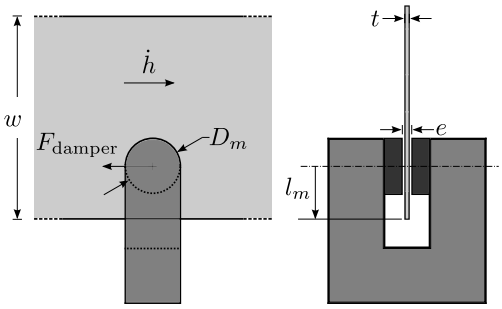

Figure A.3: Schematic of the eddy-current brake. The aluminum sliding plate, the yoke and the magnets are identified with the color varying from the lighter gray to the darker one.

In theory, the resistive force (F_{damper}) acting on the sliding plate of an eddy-current brake is given by (Wouterse, 1991):

$$F_{\text{damper}} = \left(\frac{\pi D_m^2 t B_0^2 K}{4 \rho_e} \right) \dot{h} \, , \tag{A.1}$$

where ρ_e is the electrical resistivity of the sliding plate material, namely aluminum, D_m is the magnet diameter, t is the sliding plate thickness, B_0 is the magnetic field in the middle of the gap (e) between the magnets when the plate is not moving, $\dot{h}$ is the heave velocity and K is a constant given by:

$$K = \frac{1}{2} \left[1 - \frac{\pi^2 D_m}{24 w} \right] \, , \tag{A.2}$$

with w being the width of the plate. The theoretical heave damping coefficient of the eddy-current brake ($D_{h,\text{e theory}}$) is then simply obtained by dividing the resistive force with the heave velocity:

$$D_{h,\text{e theory}} = \frac{\pi D_m^2 t B_0^2 K}{4 \rho_e} \, . \tag{A.3}$$

The various parameters characterizing the heave damper are given in Table A.6.

Table A.6: Design of the heave damper

Parameter	Value
D_m	1 in
e	1/8 in
Magnet thickness	1/2 in
Magnet material	Neodymium (N48)
w	50 mm
t	1/8 in
Plate material	Aluminum

In order to modify the heave damping coefficient, the distance between the center of the magnets and the edge of the sliding plate (see l_m in Fig. A.3) can be varied by moving the yoke so that the magnets can be shifted toward the edge of the sliding plate, thereby reducing the magnetic field passing through the plate and, at the same time, the heave damping coefficient of the eddy-current brake (see Eq. A.3). A value of $l_m = 0$ corresponds to the center of the magnets being aligned with the edge of the aluminum sliding plate, which is close to what is observed in Fig. A.2.

According to the theory (Gosline et al., 2006), the relation between the heave velocity and the resistive force generated by the eddy-current damper is linear if the heave velocity remains below a critical value. With 1/8 inch aluminum plates, this critical velocity is around 19 m/s and is well above the maximum velocity reached with the prototype during the tests conducted in the water channel.

It is important to note that the theory presented above has only been used to design the damper. The actual heave damping coefficient of the prototype has been determined following a calibration process described in Appendix B.4.

Appendix A.2. Inertial properties

The turbine has been designed to be as light as possible while being able to withstand the forces at play and to limit the deflection of the blade. To increase the heaving mass, some steel bars simply have to be added and fixed to the carriage undergoing the heaving motion. The moment of inertia and the static moment can also be altered by adding components specifically designed for that purpose, which are shown in black in Fig. A.4. Care has been taken so that the modifications of the moment of inertia and the static moment can be made independently. The moment of inertia can be increased by 28.6% with a variation of the static moment of less than 0.2% (left configuration in Fig. A.4). Then, from this increased moment of inertia value, the static moment can be reduced by 42.5% (middle configuration) or increased by 40% (right configuration) without affecting the moment of inertia. However, for all these cases, the heaving mass is increased by 4% since the components in black in Fig. A.4 need to be added to the setup.

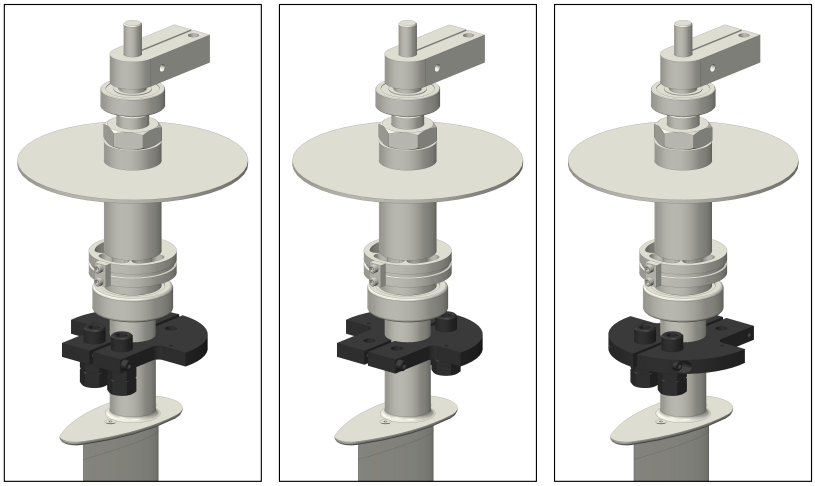

Figure A.4: Components undergoing the pitching motion.The light gray components are always present while the black components are added to the setup when one wants to increase the moment of inertia or to modify the static moment. Increased I_θ + same S (left); Increased I_θ + reduced S (middle); Increased I_θ + increased S (right).

Appendix B. Calibrations

Appendix B.1. Heave and pitch positions

The heave position is determined from the output voltage of the heave encoder using the following linear relation:

$$h = A_h \cdot \left(E_h - E_{h_i}\right) + h_i \ , \tag{B.1}$$

where A_h is the slope of the relation between the heave position (h) and the output voltage (E_h), and h_i and E_{h_i} respectively correspond to the initial heave position and the initial output voltage of the heave encoder.

The equation giving the pitch angle is analogous to Eq. B.1:

$$\theta = A_\theta \cdot \left(E_\theta - E_{\theta_i}\right) + \theta_i \ , \tag{B.2}$$

where A_θ is the calibration constant relating the output voltage of the pitch encoder (E_θ) to a pitch angle (θ), and θ_i and E_{θ_i} correspond to the initial pitch angle and the initial output voltage of the pitch encoder, respectively.

In order to determine the value of the calibration constant A_h in Eq. B.1, the heave carriage has been attached to the tool of a machining center (computer numerical control (CNC) milling machine), which allowed us to prescribe two different known heave positions (±0.09 m) with great accuracy. The value of A_h has then been obtained using the relation:

$$A_h = \frac{\left(\overline{h_2 - h_1}\right)}{\left(\overline{E_{h_2} - E_{h_1}}\right)} \, , \tag{B.3}$$

where E_h is the output voltage of the heave encoder and the subscripts 1 and 2 correspond to the two prescribed heave positions so that $\left(\overline{h_2 - h_1}\right) = 0.18$ m. The average voltage difference $\left(\overline{E_{h_2} - E_{h_1}}\right)$ has been computed from a total of 100 measurements and is equal to 3.3667 V. The resulting value of A_h is therefore:

$$A_h = 0.05346 \text{ m/V} \, . \tag{B.4}$$

The value of A_θ in Eq. B.2 has been evaluated using a similar method with the following relation:

$$A_\theta = \frac{\left(\overline{\theta_2 - \theta_1}\right)}{\left(\overline{E_{\theta_2} - E_{\theta_1}}\right)} \, . \tag{B.5}$$

The blade has been successively held at 0° and 30° pitch angles so that $\left(\overline{\theta_2 - \theta_1}\right) = 30°$. This process has been repeated 100 times in order to obtain an accurate estimation of $\left(\overline{E_{\theta_2} - E_{\theta_1}}\right)$, which is 0.2543 V. The resulting value of A_θ is then found to be equal to:

$$A_\theta = 118 \text{ degrees/V} \, . \tag{B.6}$$

Finally, note that the digital-to-analog converter has been set so that its resolution is the same as that of the encoders. In other words, one state of the 14-bit DAC corresponds to one pulse of the encoders.

Appendix B.2. Springs

A machining center has also been used to determine the stiffness of the different springs. One end of the springs was fixed to the machining center's mill table while the other end was attached to a load cell fastened to the machining center's moving tool. By prescribing different vertical positions of the tool and performing a linear regression analysis, the relation between the force measured with the load cell and the spring elongation could be found:

$$F = k\,\Delta + F_0 \, , \tag{B.7}$$

where k is the spring stiffness, Δ is the spring elongation, i.e., the distance between the position of the moving end of the spring (extended) and its initial position (not extended), F_0 is the tension force in the spring when the moving end is at its initial position and F is the tension force in the spring for a given elongation. An example of the relation between the force in a spring and its elongation is shown in Fig. B.1. It confirms the linear behavior of the springs.

Since several heave springs could be used in parallel to attach the carriage undergoing the heaving motion to the structure of the turbine, the resultant heave stiffness (k_h) in N/m is given by:

$$k_h = \sum_{i=1}^{N_h} k_i \, , \tag{B.8}$$

where N_h is the number of heave springs used for a given case and k_i is the stiffness of the i^{th} heave spring.

Regarding the resultant pitch stiffness in N.m/rad, it is given by:

$$k_\theta = (k_1 + k_2)\,\frac{D^2}{4} \, , \tag{B.9}$$

where k_1 and k_2 are the stiffness coefficients of the two extension springs used in pitch and D is the diameter of the groove in the component around which the cable linking both pitch springs is rotating, as seen in Fig. A.1.

Lastly, it is worth mentioning that some springs have been calibrated both before and after the experimental campaign in order to confirm that their stiffness coefficients remained constant over time.

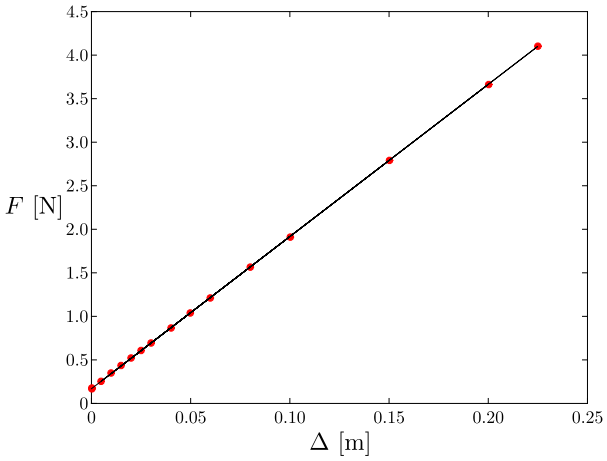

Figure B.1: Measurements of the force (F) as a function of the elongation (Δ) for a given spring (red dots) along with the linear regression curve.

Appendix B.3. Mass, moment of inertia and static moment

Free vibration tests have been performed independently in heave and in pitch (with the other degree of freedom fixed in place) at a sampling frequency of 5000 Hz to determine the mass undergoing the heaving motion (m_h) and the moment of inertia (I_θ). These tests have been conducted in ambient air so that the fluid forces are negligible compared to the friction in the bearings. The blade, the end plate and the screws needed to fasten them together and to fix them to the shaft undergoing the pitching motion were not in place during the free vibration tests in heave. As a result, only a fraction of the total heaving mass has been evaluated using this method. The remaining mass fraction has been determined by weighing the other components individually and summing their masses. The reason for not simply weighing all the components undergoing the heaving motion is that using free vibration tests is a simple and straightforward method allowing us to evaluate the equivalent mass stemming from the rotation of some components such as the linear guided roller bearings and that of the heave springs which are not moving as rigid bodies with the carriage since one of their end is attached to the fixed turbine structure.

The fraction of the heaving mass ($m_{h\,\mathrm{free}}$) present during the free vibration tests has been determined using the following relation:

$$m_{h\,\mathrm{free}} = k_h/\omega_{n,h\,\mathrm{free}}^2 \,, \tag{B.10}$$

where k_h is the heave stiffness, which is known following the calibration described in Appendix B.2, and $\omega_{n,h\,\mathrm{free}}$ is the heave natural frequency of the components present during the free vibration tests. However, as there was some viscous friction in heave even if the heave damper was not present during these tests due to presence of the linear guided roller bearings, the carriage did not exactly oscillate at its natural frequency ($\omega_{n,h\,\mathrm{free}}$), but rather at its damped natural frequency ($\omega_{d,h\,\mathrm{free}}$):

$$\omega_{n,h\,\mathrm{free}} = \frac{\omega_{d,h\,\mathrm{free}}}{\sqrt{1-\zeta_h^2}} \,, \tag{B.11}$$

where ζ_h is the damping ratio in heave, whose evaluation is described in the next subsection. The heaving mass of the components involved in the free vibration tests has therefore been computed using the equation:

$$m_{h\,\mathrm{free}} = \frac{k_h\, T_{h\,\mathrm{free}}^2 \left(1-\zeta_h^2\right)}{4\pi^2} \,, \tag{B.12}$$

where $T_{h\,\mathrm{free}}$ is the oscillation period ($T_{h\,\mathrm{free}} = 2\pi/\omega_{d,h\,\mathrm{free}}$).

The same procedure has been used to determine the moment of inertia (I_θ), resulting in the equation:

$$I_\theta = \frac{k_\theta\, T_\theta^2 \left(1-\zeta_\theta^2\right)}{4\pi^2} \,, \tag{B.13}$$

Note that, unlike the heaving mass, all the components undergoing the pitching motion were in place during the free vibration tests as the individual contribution of a single component to the total moment of inertia cannot be easily estimated. The average period evaluated from 15 to 120 complete oscillations, recorded during a few free vibration tests, have been used to evaluate the period of oscillation $T_{h\,\mathrm{free}}$, while 20 to 40 oscillations have been used for T_θ.

Determining the static moment using free vibration tests would have involved the computation of the pitch and heave accelerations which would therefore have been much less accurate than the computation of the heaving mass and the moment of inertia. Consequently, the static moment has rather been determined using a 3D computer model produced with a computer-aided design (CAD) software to localize the center of mass of each components undergoing the pitching motion. Knowing the volume of these components from the CAD and their mass using a weighing scale, their density could be computed and set in the computer model. The position of the center of mass could then be accurately evaluated from the CAD software. In order to validate this procedure, the moment of inertia has been computed from the CAD and compared to the value obtained from the free vibration tests. The difference between the values obtained from both methods is below 1% for all the different moment of inertia values.

The static moment of each component undergoing the pitching motion has been found by multiplying their mass with the distance between their center of mass and the pitch axis (x_θ) (see Fig. 1 and Table 1 for the sign convention). The total static moment is then simply given by:

$$S = \sum_{i=1}^{N_\theta} \left(m_i \, x_{\theta,i} \right) \, , \tag{B.14}$$

where N_θ is the number of components involved in the pitching motion and m_i is the mass of the i$^{\mathrm{th}}$ component undergoing the pitching motion.

Appendix B.4. Linear damping and Coulomb friction

The friction in heave and in pitch is considered to be a sum of linear (viscous) and Coulomb contributions. A simplified model of the Coulomb friction is considered for which the friction force ($f_{y\,\mathrm{Coulomb}}$) and moment ($m_{\,\mathrm{Coulomb}}$) are constant and acting in the opposite directions than the heave and pitch velocities:

$$F_{y\,\mathrm{Coulomb}} = -f_{y\,\mathrm{Coulomb}} \, \mathrm{sign}(\dot{h}) \, , \tag{B.15}$$

$$M_{\,\mathrm{Coulomb}} = -m_{\,\mathrm{Coulomb}} \, \mathrm{sign}(\dot{\theta}) \, . \tag{B.16}$$

Using this assumption and following the procedure described in the work of Feeny and Liang (1996), the linear damping and Coulomb friction contributions of a given degree of freedom can be evaluated from a single free vibration test with the other degree of freedom being held in place, as has been done to evaluate the mass and the moment of inertia (see Appendix B.3).

To determine the linear damping contribution, the parameter β has first been determined using:

$$\beta = -\frac{1}{\pi} \ln \left(-\frac{(X_{i+1} - X_{i-1})}{(X_i - X_{i-2})} \right) \, , \tag{B.17}$$

where X_i is the i^{th} peak value in heave or in pitch of a free vibration test. This parameter is then used to compute the damping ratio (ζ) of a given degree of freedom:

$$\zeta = \frac{\beta}{\sqrt{1 + \beta^2}} \, , \tag{B.18}$$

from which the linear damping coefficients in heave (D_h) and in pitch (D_θ) can be evaluated:

$$D_h = 2 \, \zeta_h \, \sqrt{k_h \, m_h} \, , \tag{B.19}$$

$$D_\theta = 2 \, \zeta_\theta \, \sqrt{k_\theta \, I_\theta} \, . \tag{B.20}$$

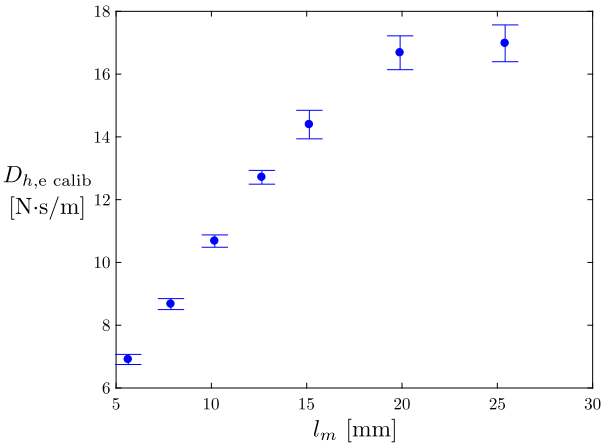

Figure B.2: Contribution of the eddy-current brake to the heave damping coefficient ($D_{h,\mathrm{e}}$) as a function of the distance between the center of the magnets and the edge of the sliding plate (l_m). Note that l_m is zero when the center of the magnets is aligned with the edge of the sliding plate and is positive when the magnets are shifted toward the center of the sliding plate (see Fig. A.3).

Note that this method allows computing the total linear damping (D_h) and therefore includes both the contribution of the eddy-current brake ($D_{h,\mathrm{e}}$) and the friction in the heave bearings ($D_{h,\mathrm{v}}$). The value of $D_{h,\mathrm{v}}$ can be easily determined as it is equal to D_h when the eddy-current brake is removed from the setup. As a result, the value of $D_{h,\mathrm{e}}$ can be evaluated for different positions of the magnets (l_m) by performing successive free vibration tests, including a case without the eddy-current brake:

$$D_{h,\mathrm{e\ calib}} = D_{h\ \mathrm{calib}} - D_{h,\mathrm{v\ calib}}\ , \tag{B.21}$$

and the results are presented in Fig. B.2.

The different positions of the magnets tested during the calibration of the eddy-current brake have been chosen to match those used during the tests conducted in the water channel. Nevertheless, the positions of the magnets were not exactly the same and a linear interpolation has been performed to obtain a more accurate value of the eddy-current brake damping during the tests in the channel for a given position of the magnets (l_m). Moreover, one can notice from the theory (see Eq. A.3) that the eddy-current brake damping varies with temperature since the magnets' magnetic field (B_0) and the electrical resistivity of aluminum (ρ_e) are temperature dependent. The eddy-current brake damping therefore needs to be corrected to take into account the temperature difference (ΔT) of the aluminum sliding plate between the time at which a given test is conducted and the time at which the calibration has been carried out. The eddy-current brake damping coefficient value for a given test is therefore given by:

$$D_{h,\mathrm{e}} = \frac{\left(1 + \alpha_{B_0}\,\Delta T\right)^2}{\left(1 + \alpha_{\rho_e}\,\Delta T\right)}\, D_{h,\mathrm{e\ calib}}\ , \tag{B.22}$$

with:

$$\Delta T = T - T_{\mathrm{calib}}\ , \tag{B.23}$$

where T is the temperature of the aluminum sliding plate during a given test, T_{calib} is its temperature during the calibration process (25.5 °C), $D_{h,\mathrm{e\ calib}}$ is the linearly interpolated eddy-current brake damping coefficient evaluated during the calibration for a given position of the magnets, α_{B_0} is the temperature coefficient of the magnetic field given by (Pyrhonen et al., 2014):

$$\alpha_{B_0} = -0.0012\ {}^{\circ}C^{-1}\ , \tag{B.24}$$

and α_{ρ_e} is the temperature coefficient of the electrical resistivity, which has a value of (Haynes, 2015):

$$\alpha_{\rho_e} = 0.0044\ {}^{\circ}C^{-1}\ , \tag{B.25}$$

around 24.85°C.

Note that the variations of the ambient temperature during the experimental campaign, which took place over several weeks, have resulted in a maximum difference between the ambient temperature during a test and the ambient temperature during the calibration of approximately 4 °C, which corresponds to a variation of the damping coefficient by less than 3%.

Since most of the energy extracted from the flow is dissipated into heat in the aluminum sliding plate of the eddy-current brake, an increase of the aluminum sliding plate temperature during a single test would not have been surprising. However, the plate temperature has been measured with an infrared thermometer at the beginning and at the end of every test conducted in the channel, each lasting 2 minutes, and the temperature difference was always equal or below 0.2 °C. Consequently, the eddy-current brake damping can be considered to be constant during a given test since its variation due to the temperature differences occurring during a single test is below 0.1%, which is smaller than the damping coefficient uncertainty.

Regarding the Coulomb friction contributions, the constant friction force and moment (See Eqs. B.15 and B.16) are given by:

$$f_{y\,\mathrm{Coulomb}} = C_h\, k_h \ , \tag{B.26}$$

$$m_{\,\mathrm{Coulomb}} = C_\theta\, k_\theta \ , \tag{B.27}$$

where C_h and C_θ are Coulomb friction parameters that are evaluated using the following equation with the corresponding variables in heave and in pitch:

$$C = \frac{\left[(X_{i+1} - X_i) + \mathrm{e}^{-\beta\pi}\,(X_i - X_{i-1})\right]}{2\left(1 + \mathrm{e}^{-\beta\pi}\right)} \ , \tag{B.28}$$

These formulations eliminate the bias that would arise from nonzero equilibrium positions in heave and in pitch since subtractions of successive positive and negative peak values are used in Eqs. B.17 and B.28. Moreover, these two equations have been generalized to consider all the peak values from each free vibration tests instead of just two pairs of successive peaks. Lastly, the aerodynamic drag of the turbine components located above the water has been found to be negligible compared to the friction in the bearings, even when considering the largest velocities that have been reached during the whole experimental campaign.

Appendix C. Validation of the calibrations

In order to validate the parameter values determined from the calibrations, the equations of motion (Eqs. 3 and 4) have been solved numerically with second-order schemes and the results have been compared with free vibration tests carried out with the experimental setup. These tests have been conducted in ambient air and without the blade. Consequently, the numerical solver did not need to solve the Navier-Stokes equations because the aerodynamic drag (in the air) of the remaining moving components is negligible compared to the other contributions in the equations of motion. First, the results from one-degree-of-freedom free vibration tests in heave and in pitch are presented in Figs. C.1 and C.2.

As the frequencies of the experimental signals agree well with those of the numerical solutions, one can conclude that the evaluation of the heaving mass (m_h), the heave stiffness (k_h), the moment of inertia (I_θ) and the pitch stiffness (k_θ) are accurate. Furthermore, the fact that the amplitudes also agree well with each other validate that the estimations of the linear damping and Coulomb friction contributions are also correct. This leaves the evaluation of the static moment which could not be confirmed with a 1-DOF free vibration test since this parameter couples the heaving and the pitching motions. A 2-DOF free vibration in the air has therefore been carried out and the results are presented in Fig. C.3. Once again, a good match between the experimental results and the numerical simulation is observed for both degrees of freedom, hence confirming that all the structural parameters have been correctly evaluated.

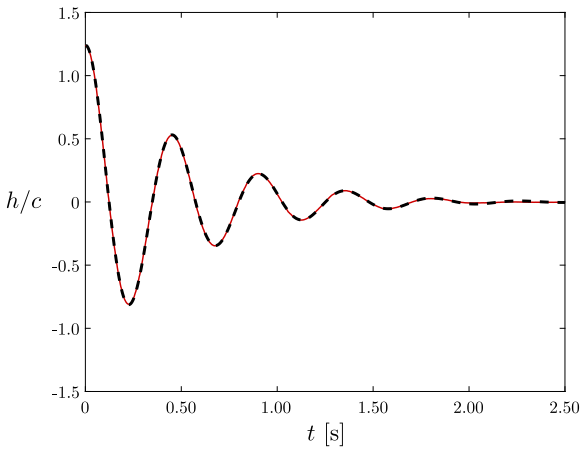

Figure C.1: Comparison between the experimental data (solid red line) and the numerical solution (dashed black line) of a free vibration test in heave with the blade being held at $\theta = 0°$. $m_h = 2.54$ kg; $D_h = 9.4$ N.s/m; $k_h = 503.4$ N/m; $f_{y\,\text{Coulomb}} = 0.1$ N.

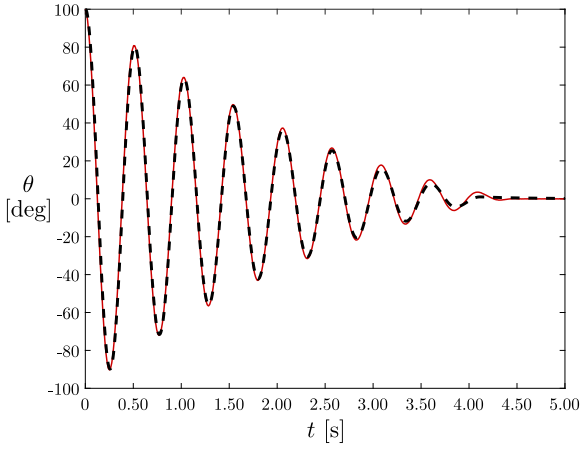

Figure C.2: Comparison between the experimental data (solid red line) and the numerical solution (dashed black line) of a free vibration test in pitch with the blade being held at $h/c = 0$. $I_\theta = 2.23\times10^{-4}$ Kg.m^2; $D_\theta = 1.28\times10^{-4}$ N.m.s/rad; $k_\theta = 0.0333$ N.m/rad; $m_{\,\text{Coulomb}} = 9\times10^{-4}$ N.m.

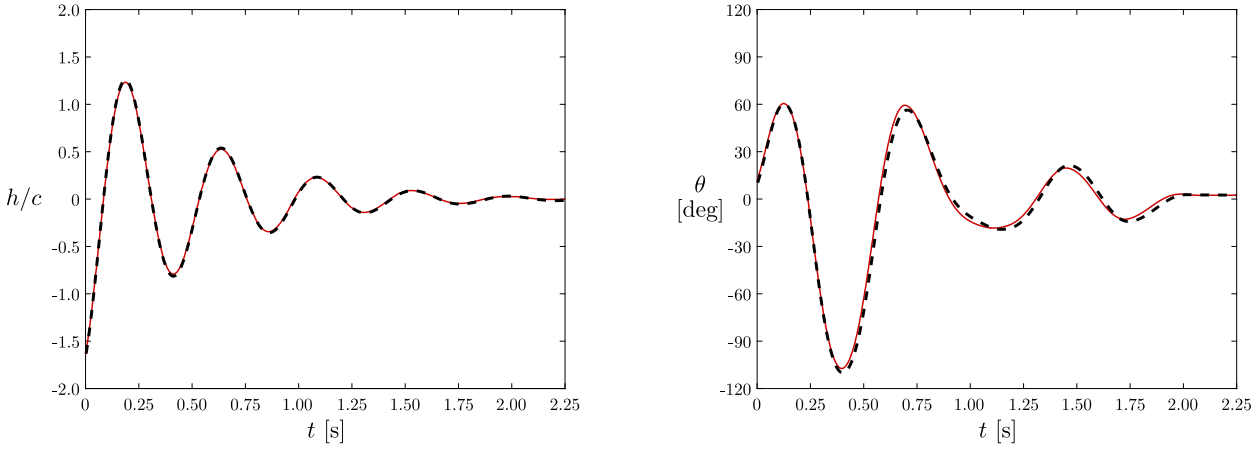

(a) Heave

(b) Pitch

Figure C.3: Comparison between the experimental data (solid red lines) and the numerical solution (dashed black lines) of a free vibration test involving both degrees of freedom. m_h = 2.54 kg, I_θ = 1.01 × 10^{-4} Kg.m^2, S = −0.00131 kg.m; D_h = 9.4 N.s/m; k_h = 503.4 N/m; k_θ = 0.0097 N.m/rad; D_θ = 3.8 × 10^{-5} N.m.s/rad; $f_{y\,\text{Coulomb}}$ = 0.1 N; $m_{\,\text{Coulomb}}$ = 9 × 10^{-4} N.m.

References

Abiru, H., Yoshitake, A., 2011. Study on a Flapping Wing Hydroelectric Power Generation System. Journal of Environment and Engineering 6 (1), 178–186.

Abiru, H., Yoshitake, A., 2012. Experimental Study on a Cascade Flapping Wing Hydroelectric Power Generator. Journal of Energy and Power Engineering 6 (9), 1429–1436.

Amandolese, X., Michelin, S., Choquel, M., 2013. Low speed flutter and limit cycle oscillations of a two-degree-of-freedom flat plate in a wind tunnel. Journal of Fluids and Structures 43, 244–255.

Deng, J., Teng, L., Pan, D., Shao, X., 2015. Inertial effects of the semi-passive flapping foil on its energy extraction efficiency. Physics of Fluids 27 (5), 053103 (17 pp.) –.

Derakhshandeh, J., Arjomandi, M., Dally, B., Cazzolato, B., 2016. Flow-induced vibration of an elastically mounted airfoil under the influence of the wake of a circular cylinder. Experimental Thermal and Fluid Science 74, 58 – 72.

Dowell, E. H., 2004. A Modern Course in Aeroelasticity Fourh Revised and Enlarged Edition, 4th Edition. Kluwer Academic Publishers, Dordrecht, The Netherlands.

Farthing, S. P., 2013. Binary flutter as an oscillating windmill scaling & linear analysis. Wind Engineering 37 (5), 483–499.

Feeny, B., Liang, J., 1996. A decrement method for the simultaneous estimation of coulomb and viscous friction. Journal of Sound and Vibration 195 (1), 149 – 154.

Fung, Y., 2008. An Introduction to the Theory of Aeroelasticity. Dover Publications, Mineola, New York, USA.

Gosline, A. H., Campion, G., Hayward, V., 2006. On the Use of Eddy Current Brakes as Tunable, Fast Turn-On Viscous Dampers For Haptic Rendering. In: Proc. Eurohaptics 2006. pp. 229–234.

Griffith, M. D., Jacono, D. L., Sheridan, J., Leontini, J. S., 2016. Passive heaving of elliptical cylinders with active pitching from cylinders towards flapping foils. Journal of Fluids and Structures 67, 124 – 141.

Haynes, W., 2015. CRC Handbook of Chemistry and Physics, 96th Edition. CRC Press, Boca Raton, FL, USA.

Huxham, G. H., Cochard, S., Patterson, J., 2012. Experimental Parametric Investigation of an Oscillating Hydrofoil Tidal Stream Energy Converter. In: Proceedings of the 18th Australasian Fluid Mechanics Conference. Launceston, Australia.

Kim, D., Strom, B., Mandre, S., Breuer, K., 2017. Energy harvesting performance and flow structure of an oscillating hydrofoil with finite span. Journal of Fluids and Structures 70, 314 – 326.

Kinsey, T., Dumas, G., 2008. Parametric Study of an Oscillating Airfoil in a Power-Extraction Regime. AIAA Journal 46 (6), 1318–1330.

Kinsey, T., Dumas, G., 2012. Computational Fluid Dynamics Analysis of a Hydrokinetic Turbine Based on Oscillating Hydrofoils. Journal of Fluids Engineering 134 (2), 021104 (16 pp.) –.

Kinsey, T., Dumas, G., 2014. Optimal Operating Parameters for an Oscillating Foil Turbine at Reynolds Number 500,000. AIAA Journal 52 (9), 1885–1895.

Kinsey, T., Dumas, G., Lalande, G., Ruel, J., Mehut, A., Viarouge, P., Lemay, J., Jean, Y., 2011. Prototype testing of a hydrokinetic turbine based on oscillating hydrofoils. Renewable Energy 36 (6), 1710 – 1718.

McKinney, W., DeLaurier, J., 1981. Wingmill: An Oscillating-Wing Windmill. Journal of Energy 5 (2), 109–115.

Munson, B. R., Okiishi, T. H., Huebsch, W. W., Rothmayer, A. P., 2013. Fundamentals of fluid mechanics, 7th Edition. John Wiley & Sons, Hoboken, NJ, USA.

Peng, Z., Zhu, Q., 2009. Energy harvesting through flow-induced oscillations of a foil. Physics of Fluids 21 (12), 174–191.

Pigolotti, L., Mannini, C., Bartoli, G., Thiele, K., 2017. Critical and post-critical behaviour of two-degree-of-freedom flutter-based generators. Journal of Sound and Vibration 404, 116 – 140.

Pyrhonen, J., Jokinen, T., Hrabovcová, V., 2014. Design of rotating electrical machines, 2nd Edition. Wiley, Chichester, West Sussex, United Kingdom.

Shimizu, E., Isogai, K., Obayashi, S., 2008. Multiobjective Design Study of a Flapping Wing Power Generator. Journal of Fluids Engineering 130 (2), 021104 (8 pp.) –.

Sitorus, P. E., Le, T. Q., Ko, J. H., Truong, T. Q., Park, H. C., 2015. Design, implementation, and power estimation of a lab-scale flapping-type turbine. Journal of Marine Science and Technology.

Spalart, P. R., Allmaras, S. R., 1994. A One-Equation Turbulence Model for Aerodynamic Flows. Recherche Aérospatiale (1), 5–21.

Teng, L., Deng, J., Pan, D., Shao, X., 2016. Effects of non-sinusoidal pitching motion on energy extraction performance of a semi-active flapping foil. Renewable Energy 85, 810 – 818.

Veilleux, J.-C., 2014. Optimization of a Fully-Passive Flapping-Airfoil Turbine. Master's thesis, Université Laval, Québec, Québec, Canada.

Veilleux, J.-C., Dumas, G., 2017. Numerical optimization of a fully-passive flapping-airfoil turbine. Journal of Fluids and Structures 70, 102 – 130.

Wang, Z., Du, L., Zhao, J., Sun, X., 2017. Structural response and energy extraction of a fully passive flapping foil. Journal of Fluids and Structures 72, 96 – 113.

Wouterse, J., 1991. Critical torque and speed of eddy current brake with widely separated soft iron poles. Electric Power Applications, IEE Proceedings B 138 (4), 153–158.

Wu, J., Chen, Y. L., Zhao, N., 2015. Role of induced vortex interaction in a semi-active flapping foil based energy harvester. Physics of Fluids 27 (9), 093601.

Wu, J., Qiu, Y. L., Shu, C., Zhao, N., 2014. Pitching-motion-activated flapping foil near solid walls for power extraction: A numerical investigation. Physics of Fluids 26 (8), 083601.

Xiao, Q., Zhu, Q., 2014. A review on flow energy harvesters based on flapping foils. Journal of Fluids and Structures 46, 174–191.

Xu, G., Xu, W., Dai, J., 2017. Numerical and experimental study of a flapping foil generator. Applied Ocean Research 63, 242 – 250.

Young, J., Lai, J. C. S., Platzer, M. F., 2014. A review of progress and challenges in flapping foil power generation. Progress in Aerospace Sciences 67, 2–28.

Zhan, J., Xu, B., Wu, J., Wu, J., 2017. Power extraction performance of a semi-activated flapping foil in gusty flow. Journal of Bionic Engineering 14 (1), 99 – 110.

Zhu, Q., 5 2011. Optimal frequency for flow energy harvesting of a flapping foil. Journal of Fluid Mechanics 675, 495–517.
Zhu, Q., 2012. Energy harvesting by a purely passive flapping foil from shear flows. Journal of Fluids and Structures 34, 157–169.
Zhu, Q., Haase, M., Wu, C. H., 2009. Modeling the capacity of a novel flow-energy harvester. Applied Mathematical Modelling 33 (5), 2207–2217.
Zhu, Q., Peng, Z., 2009. Mode coupling and flow energy harvesting by a flapping foil. Physics of Fluids 21 (3), 033601 (10 pp.) –.